

Nup62 is recruited to pathological condensates and promotes TDP-43 insolubility in C9orf72 and sporadic ALS/FTLD.

Amanda Gleixner

University of Pittsburgh Medical Center

Brandie Morris Verdone

Thomas Jefferson University

Charlton Otte

University of Pittsburgh

Nandini Ramesh

University of Pittsburgh Medical Center

Jenna Gale

University of Pittsburgh <https://orcid.org/0000-0003-2727-9497>

Jocelyn Mauna

University of Pittsburgh

Jacob Mann

University of Pittsburgh

Katie Copley

University of Pittsburgh

Elizabeth Daley

Northwestern University <https://orcid.org/0000-0003-2342-452X>

Juan Ortega

The Ken & Ruth Davee Department of Neurology, Northwestern University Feinberg School of Medicine, Chicago, IL, 60611

Maria Cicardi

Thomas Jefferson University

Evangelos Kiskinis

The Ken & Ruth Davee Department of Neurology, Northwestern University Feinberg School of Medicine, Chicago, IL, 60611 <https://orcid.org/0000-0001-8342-8616>

Julia Kofler

University of Pittsburgh

Udai Pandey

University of Pittsburgh Medical Center

Davide Trotti

Thomas Jefferson University
Christopher Donnelly (✉ cjdon25@pitt.edu)
University of Pittsburgh

Article

Keywords: Amyotrophic lateral sclerosis (ALS), Frontotemporal Lobar Degeneration (FTLD)

Posted Date: February 19th, 2021

DOI: <https://doi.org/10.21203/rs.3.rs-144654/v1>

License: © ⓘ This work is licensed under a Creative Commons Attribution 4.0 International License.
[Read Full License](#)

Version of Record: A version of this preprint was published at Nature Communications on June 13th, 2022. See the published version at <https://doi.org/10.1038/s41467-022-31098-6>.

Nup62 is recruited to pathological condensates and promotes TDP-43 insolubility in C9orf72 and sporadic ALS/FTLD.

Amanda M. Gleixner^{1,2}, Brandie Morris Verdone³, Charlton G. Otte^{1,2,4}, Nandini Ramesh^{5,6}, Jenna Gale^{1,2}, Jocelyn D. Mauna^{1,2}, Jacob R. Mann^{1,2,7}, Katie E. Copley^{1,2}, Elizabeth L. Daley⁸, Juan A. Ortega⁸, Maria Elena Cicardi³, Evangelos Kiskinis^{8,9}, Julia Kofler^{2,10}, Udai B. Pandey^{2,6,7}, Davide Trotti³, Christopher J. Donnelly^{1,2,7}

Correspondence: chrisdonnelly@pitt.edu; cjdon25@pitt.edu

Affiliations:

1. Department of Neurobiology, University of Pittsburgh School of Medicine, Pittsburgh, PA, USA
2. LiveLikeLou Center for ALS Research, University of Pittsburgh Brain Institute, Pittsburgh, PA, USA
3. Department of Neuroscience, Jefferson Weinberg ALS Center, Vickie and Jack Farber Institute for Neuroscience, Thomas Jefferson University, Philadelphia, PA, USA
4. Physician Scientist Training Program, University of Pittsburgh School of Medicine, Pittsburgh, PA, USA
5. Department of Human Genetics, University of Pittsburgh Graduate School of Public Health, Pittsburgh, PA, USA
6. Department of Pediatrics, Children's Hospital of Pittsburgh, University of Pittsburgh Medical Center, Pittsburgh, PA, USA
7. Center for Neuroscience, University of Pittsburgh, Pittsburgh, PA, USA
8. The Ken & Ruth Davee Department of Neurology, Northwestern University of Feinberg School of Medicine, Chicago, IL, USA
9. Department of Physiology, Northwestern University Feinberg School of Medicine, Chicago, IL, USA
10. Department of Pathology, University of Pittsburgh, Pittsburgh, PA, USA.

Highlights

- Nup62 is a genetic modifier of retinal neurodegeneration in C9-ALS/FTLD *Drosophila* models.
- Poly-GR accumulation drives Nup62 to cytoplasmic TDP-43⁺ stress granules.
- Cytoplasmic Nup62 triggers cytoplasmic insoluble TDP-43 inclusions.
- Deleterious phase transitions recruit Nup62 to phosphorylated TDP-43 inclusions.

Abstract

Amyotrophic lateral sclerosis (ALS) and Frontotemporal Lobar Degeneration (FTLD) share clinical, neuropathological, and genetic features. This includes common genetic disease-causing mutations such as the expanded G4C2 repeat in the *C9orf72* gene (C9-ALS/FTLD) and cytoplasmic and insoluble protein depositions of the TDP-43 in degenerating regions of the brain and spinal cord. Proposed mechanisms of toxicity in C9-ALS/FTLD are the production of repeat expansion transcripts and their dipeptide repeat proteins (DPRs) products which are hypothesized to drive nucleocytoplasmic transport defects. The nuclear pore complex (NPC) regulates nucleocytoplasmic trafficking by creating a selectivity and permeability barrier comprised of phenylalanine glycine nucleoporins (FG nups). However, the relationship between FG nups and TDP-43 pathology remains elusive. Here, we define two mechanisms through which TDP-43 promotes Nup62 nuclear depletion and cytoplasmic in C9-ALS/FTLD and sALS/FTLD. In C9-ALS/FTLD, poly-GR initiates the formation of TDP-43 containing stress granules (SGs) that trigger the nuclear loss and recruitment of Nup62 *in vitro* and *in vivo*. When colocalized, cytoplasmic TDP-43:Nup62 assemblies mature into insoluble inclusions through an interaction within the TDP-43 nuclear localization sequence (NLS) suggesting Nup62 promotes deleterious phase transitions. Absent of poly-GR, aberrant TDP-43 phase transitions in the cytoplasm recruits and mislocalizes Nup62 into pathological inclusions. The result of these cytoplasmic Nup62 and TDP-43 interactions are pathological and insoluble TDP-43:Nup62 assemblies that are observed in C9-ALS/FTLD and sALS/FTLD CNS tissue.

Introduction

ALS and FTLN are fatal neurodegenerative disorders that share neuropathological features and causative mutations and are considered to exist along a disease spectrum^{1,2}. TDP-43 and FUS are predominantly nuclear RNA-binding proteins (RBPs) that cycle between the nucleus and cytoplasm and primarily regulate RNA metabolism³. However, these proteins mislocalize to the cytoplasm and form inclusions in the vast majority of ALS patients and up to half of FTLN patients⁴⁻⁹. In addition to shared neuropathology, the most common genetic cause of both ALS and FTLN is an expanded G4C2 hexanucleotide repeat sequence in the first intron of the *C9orf72* gene (C9-ALS/FTLN)¹⁰⁻¹³. The disease-causing pathobiology underlying this mutation includes various consequences of the expanded allele: *C9orf72* haploinsufficiency, the deposition of toxic repetitive RNAs, and accumulation of dipeptide repeats (DPRs)^{10,14-20}.

While the causative mechanism driving C9-ALS/FTLN pathobiology remains unclear, recent work suggests that *C9orf72* haploinsufficiency alone is not sufficient to initiate motor or cognitive phenotypes in rodent models²¹. However, complete loss of both alleles causes mild motor impairment as shown by reduced activity on the open-field test²²⁻²⁴. In contrast, expression of an expanded G4C2 sequence drives neurotoxicity *in vitro*^{25,26} and cognitive phenotypes *in vivo* in AAV and BAC transgenic rodent models^{23,27-30}. Further, *C9orf72* protein knockdown in two G4C2 repeat expansion mouse models caused a synergistic increase in cognitive defects and neurotoxicity to support the convergence of loss and gain of function mechanisms of toxicity^{31,32}.

C9-ALS/FTLN gain-of-function toxicity from the G4C2 expansion includes RNA:protein accumulations that manifest as RNA foci^{10,33} that sequester RBPs and impair their normal function^{15,33-38}. Furthermore, expanded repetitive RNAs are translated into five DPRs from both G4C2 sense and C4G2 antisense strands through the non-canonical repeat associated non-ATG translation (RANT) pathway³⁹⁻⁴¹. These DPRs include: glycine-arginine (GR), glycine-alanine (GA), proline-arginine (PR), proline-alanine (PA), and glycine-proline (GP)⁴²⁻⁴⁵. Both RNAs and

DPRs are found in patient derived C9-ALS/FTLD iPSC-derived neuronal cultures^{15,16,46} and post-mortem tissue samples^{10,33,47,48}. While it is difficult to distinguish between RNA-mediated toxicity in the absence of DPRs and that due to the production of DPRs, both products are thought to contribute to C9-ALS/FTLD pathobiology. Expression of codon-optimized sequences encoding DPRs cause excitotoxicity in neurons, alters nucleolar and mitochondrial functions, disrupts SG dynamics, causes ribosomal disfunction and are cytotoxic⁴⁹⁻⁵⁸. However, perhaps the most highlighted cellular biology disrupted in C9-ALS/FTLD is the nucleocytoplasmic transport pathway⁵⁹⁻⁶⁶.

Nucleocytoplasmic transport refers to the trafficking of proteins and RNAs across the nuclear membrane through the NPC⁶⁷. The NPC is a large multi-subunit protein complex comprised of approximately 30 different protein subunits, known as nucleoporins or nups⁶⁸. Nups serve a variety of functions but their most well-defined role involves creating the NPC permeability and selectivity barrier⁶⁹⁻⁷¹. Molecules smaller than 40 kDa can freely diffuse across the NPC⁷². Facilitated nucleocytoplasmic transport of larger molecules is driven by a gradient of Ran:GTP⁷³⁻⁷⁷, and larger molecules are escorted through the NPC by nuclear transport receptors, or karyopherins, which traverse the pore by interacting with FG nucleoporins (FG nups)⁷⁸⁻⁸². FG nups make up approximately one-third of the NPC nucleoporins and contain protein domains that are enriched in phenylalanine (F)-glycine (G) residues, amino acid residues associated with structural disorder and flexibility^{83,84}. This enrichment of phenylalanine and glycine creates intrinsically disordered regions (IDRs) within FG nups that, in turn, contribute to the NPC permeability barrier by forming a hydrogel-like structure through liquid-liquid phase separation^{85,86}.

The impact of G4C2 repeat expansion expression on nucleocytoplasmic trafficking is well documented in a variety of model systems. Initial studies employing RNAi and chromosomal deletion genetic screens to identify modifiers of UAS-G4C2-30 repeat and UAS-G4C2-58 repeat toxicity in *Drosophila* retinal neurons (GMR-GAL4 driven expression) revealed several genes of

the nucleocytoplasmic transport pathway and NPC, such as FG nups, as potent modifiers of toxicity^{59,63}. Furthermore, karyopherin overexpression was identified as a strong suppressor of PR₅₀ toxicity in a yeast genetic screen⁶². Similarly, downregulation of several karyopherins and Ran gradient regulators enhanced degenerative eye phenotype in a PR₂₅-expressing *Drosophila* model⁶¹ and GR₅₀- expressing *Drosophila*⁵³. In addition to genetic screens using invertebrate model systems, impaired nucleocytoplasmic trafficking dynamics are well documented in C9-ALS/FTLD iPSC-derived neurons and regulators of transport were subsequently shown to exhibit abnormal staining in post-mortem tissue^{59,87,88}. Non-FG nup irregularities were also observed in C9-ALS patient post-mortem motor cortex samples^{59,88}. The underlying hypothesis regarding C9-ALS/FTLD and nucleocytoplasmic trafficking is that perturbations promote the mislocalization of TDP-43 or FUS proteins and while there is mounting evidence of nucleocytoplasmic trafficking impairment, the mechanisms linking FG Nups to cellular dysfunction and neuropathology remain undefined.

Here we examined the relationship between C9-ALS/FTLD pathobiology and FG nups using multiple *in vitro* and *in vivo* model systems. In this study, we show that FG nups are genetic modifiers of neurotoxicity in C9-ALS/FTLD *Drosophila* models and that Nucleoporin p62 (Nup62), the most abundant FG nup within the NPC that contains extensive FG-repeat tracks, is a potent enhancer of expanded GR toxicity. Cellular GR accumulation disrupts the nuclear localization of Nup62 and promotes its cytoplasmic accumulation *in vitro* and *in vivo*. Furthermore, cytoplasmic poly-GR accumulation induces the formation of TDP-43 containing SGs that recruit Nup62 protein and cytoplasmic TDP-43 inclusions, formed through aberrant liquid-liquid phase separation, also sequester Nup62 proteins independent of SGs. Cytoplasmic Nup62 and TDP-43 interactions promote soluble-to-insoluble transition of these protein assemblies that is dependent on the TDP-43 nuclear localization sequence (NLS). Analyses of post-mortem tissue validates phosphorylated TDP-43:Nup62 in C9-ALS/FTLD and sporadic ALS/FTLD cases. Collectively,

this study defines two mechanisms by which cytoplasmic TDP-43 sequesters Nup62 and promotes the formation of pathological inclusions: GR-induced stress granules and phase separated cytoplasmic TDP-43 condensates.

Materials and Methods

Drosophila studies

Drosophila stocks: Fly stocks and crosses were maintained on standard cornmeal medium in light/dark controlled incubators. RNAi flies were obtained from VDRC or the Transgenic RNAi project⁸⁹ via Bloomington DGRC. The Nup62 overexpression fly was generated by the BestGene Inc methodology we used previously^{90–92}. UAS-(G4C2)₃₀ was kindly shared with our lab by Peng Jin³⁴ and UAS-(G4C2)₃₆ and UAS-GR₃₆ flies were generous gifts from Adrian Isaac's lab⁴⁸

Nup RNAi screen: UAS-RNAi virgin females were crossed with recombinant GMR-GAL4/UAS-(G4C2)₃₀ males or control GMR-GAL4/UAS-EGFP males at 28°C. Female progenies of the appropriate genotype were collected and their eyes were imaged with a Leica M205C digital camera at 0-1 days post-eclosion, with at least 15 eyes imaged per tested RNAi. Images of external eye phenotype were then scored as previously described⁹³.

Nup62 RNAi and G4C2 toxicity characterization: GMR-GAL4/UAS-(G4C2)₃₆ males were crossed with Nup62 RNAi virgin females at 25°C and imaged/quantified. Eclosion defects were noted in these flies, therefore we quantified the number of eclosed and unclosed flies each evening per 24 h period, across at least 5 days of three independent sets of crosses. GMR-GAL4/UAS-(G4C2)₃₆ males were crossed with Nup62 OE virgin females and external eyes were imaged and quantified as described above. Recombinant GMR-GAL4/UAS Nup62 RNAi and GMR-GAL4/UAS-Nup62 overexpression lines were generated and crossed with previously described

UAS-GR₃₆⁹⁴ or an UAS-EGFP control⁵⁴ at 25°C. As described earlier, eyes were imaged within 24 h of eclosion and at least 15 eyes were imaged per condition for quantification.

Cell Culture

HEK293 cells (ATCC) were maintained in DMEM (Thermo Fisher Scientific, Cat. No. 10313039) supplemented with 10% Hyclone Bovine Growth Serum (GE Healthcare Life Sciences, Cat. No. SH3054103HI), and 1x Glutamax (Thermo Scientific, Cat. No. 35050079) at 37°C, 5% CO₂ regulated tissue culture incubator. Cells were plated on Collagen I Rate Protein, Tail (50 µg/mL, Thermo Fisher Scientific A1048301) coated glass for experiments requiring immunocytochemistry or plastic for Western blot lysates and cell death assays. Cells were transfected with 250 ng dipeptide repeat protein (50 repeat), and 150 ng optoTDP43 constructs at 80-90% confluency with Lipofectamine 3000 (Life Technologies, Cat. No. L3000001) for 24 h timepoints. Cell death was measured by Pierce LDH Cytotoxicity Assay kit according to the manufacturer's protocol (Thermo Scientific, Cat. No. 88954). For optoTDP43 experiments: cells were transfected as described above and 4 h following transfection were exposed to blue-light in tissue culture incubator (37°C, 5% CO₂) for a 16-24 h time period. Dipeptide repeat protein expression plasmid DNA were kindly provided by Davide Trotti.

Induced pluripotent stem cell maintenance and motor neuron differentiation

Induced pluripotent stem cells (iPSCs) lines studied are described in Supplemental Table 2. iPSCs were maintained in mTeSR1 medium and cells exhibiting characteristics of spontaneous differentiation were removed prior to initiating differentiation protocol. Motor neuron differentiation was conducted as previously described^{65,95}. Briefly, iPSC colonies were dissociated into a single cells suspension and plated at approximately 1,000,00 cells per well on a 6-well plate. iPSCs were then differentiated towards a motor neuron phenotype over the course of two stages. Both stages of iPSC differentiation consist of daily media changes and supplementation of N2B27 base

media (50% DMEM F12, 50% Neurobasal, 1x NEAA, 1x Glutamax, 1x N2, 1x B27). The first stage of neuroectoderm induction (6 days) occurs once the plated iPSCs reach 90% confluency are treated with N2B27 base media supplemented with 10 μ M SB431542, 100 nM LDN-193189. To mimic the signaling pattern of the ventral and posterior region of neural tube where motor neuron progenitors are located, media is also supplemented with 1 μ M Retinoic Acid and 1 μ M Smoothed Agonist. In the second stage (8 days) of neuronal differentiation, cultures are fed with N2B27 base media supplemented with SU5402 and 10 μ M DAPT. Patterning small molecules (Retinoic Acid and Smoothed Agonist) are also added to the media to assure the generation of spinal motor neurons. After the two-stage differentiation is completed, cells are dissociated and plated in NBM media (Neurobasal, 1x NEAA, 1x Glutamax, 1x N2, and 1x B27) supplemented with 0.2 μ g/mL Ascorbic Acid, 10 ng/mL BDNF, 10 ng/mL GDNF, 10 ng/mL CNTF.

Immunohistochemistry staining and human tissue analysis

Human tissue from control, sporadic and C9orf72 ALS cases was obtained from the University of Pittsburgh Neuropathology Department Brain Bank and cases are described in Supplemental Table 3. Paraffin embedded tissue sections from the cervical spinal cord, hippocampus, and cortex were stained with Nup62 (BD Biosciences, 610497, 1:100), TDP43 1D3 (Millipore Sigma, Cat. No. MABN14) and/or FUS according as previously described⁹⁶. Fluorescent images were captured with 60x objective on Nikon A1R confocal microscope. Nup62 secondary antibody was 488/FITC while phospho-TDP43 and FUS were labeled with 594/TRITC/Cy3 to ensure any localized signal detected was not due to bleed through between channels.

Poly-GR mouse studies

All procedures involving mice were approved by the Institutional Animal Care and Use Committee at Thomas Jefferson University. A knock-in F.A.S.T. cassette⁹⁷ at the ROSA26 locus^{98,99} under the ROSA26 promoter^{98,100} was used for successful integration of FLAG-GR50-GFP or FLAG-

GFP. GR50 was encoded by a randomized codon sequence to allow for production of the protein product absent of repeat-rich RNA. Animals were generated at Ingenious Targeting Laboratory, with successful knock-in confirmed via PCR from tail DNA samples. To elicit GR50/GFP expression, mice were crossed with CAG-Cre to allow for excision of STOP codon. CAG-Cre mice were a generous gift from Dr. Yuichi Obata, Riken BioResource Center, Japan. All mice are on a C57BL/6 background.

Mice were anesthetized and perfused by transcardial puncture with PBS and chilled 4% paraformaldehyde (PFA). Spinal cord was immediately dissected and post-fixed in 4% PFA for 24 hours, phosphate buffer for 24 hours, and then 30% sucrose solution for a minimum of 48 hours until proper cryoprotection was ensured (ie. sample no longer floated). Spinal cord was embedded in O.C.T. Compound (Sakura, 4583) embedding medium. Samples were sectioned serially in the transverse orientation at a thickness of 30 μm and collected on glass slides. Slides were stored at -20°C until analysis. Frozen sections were processed for immunofluorescent confocal microscopy as previously described¹⁰¹ with modifications. Briefly, spinal cord sections were rinsed with PBS prior to a 20-minute permeabilization with 0.5% T-X100 in HMK buffer (20 mM HEPES, pH 7.5, 1 mM MgCl_2 , 100 mM KCl). Sections were blocked in 10% normal donkey serum, 1% BSA in HMK buffer for 30 minutes. Sections were incubated with the following primary antibodies for approximately 18 hours at 4°C with gentle rotating: anti-nucleoporin p62 (BD Biosciences 610497, ms 1:400); anti-GFP (Millipore Sigma AB16901, chk 1:2500); and anti-NeuN (Cell Signaling Technology 24307, rb 1:200). Following 3x rinse in HMK buffer, sections were incubated with the following secondary antibodies at 1:500 each: Alexa Fluor 647 goat-anti-mouse (Thermo Fisher A32728), Alexa Fluor 546 donkey-anti-rabbit (Thermo Fisher A10040), and Alexa Fluor 488 goat-anti-chicken (Thermo Fisher A11039) for 1.5 h in HMK buffer with 1% BSA. Sections were rinsed 4x for 10 minutes each in HMK buffer at room temperature with gentle rotating, followed by 1x rinse in water and mounted in VectaShield mounting medium with DAPI

(Vector). Imaging and quantification were done on a Nikon A1R-SI confocal microscope using NIS Elements software.

Immunocytochemistry

Cells were fixed in 4% paraformaldehyde. Following several 1x phosphate buffered saline (PBS) washes, the cells were permeabilized in 0.3% TritonX-100 in 1x PBS before blocking in 5% normal donkey serum in 1x PBS with 0.3% TritonX-100 and incubated with primary antibody solution (10% normal donkey serum, 0.3% TritonX-100) overnight at 4°C. Another set of 1x PBS washes was then conducted prior to a 1 h secondary antibody (10% normal donkey serum, 0.3% TritonX-100) incubation. Coverslips were then washed with 1x PBS and mounted with Prolong Diamond with or without DAPI stain prior to microscopy imaging. Primary antibodies: MAb414 (1:1000, Biologend, Cat. No. 902901), Nup62 (1:400, Abcam, Cat. No. ab188413 or 1:500, Millipore, Mabe1043), MAP2 (1:1000, Synaptic Systems, Cat. No. 188044), Nup153 (1:300, Abcam, Cat. No. ab84872), TDP-43 (1:200, Proteintech, Cat. No.12892-1-AP), Ataxin-2 (1:400, Proteintech, Cat. No. 21776-1-AP), G3BP1 (1:300, Santa Cruz, Cat. No. sc-365338). Secondary antibodies: Donkey anti-Mouse (1:1000, Jackson Immunoresearch), Donkey anti-Rat (1:1000, Jackson Immunoresearch), Donkey anti-Guinea Pig (1:1000, Jackson Immunoresearch), Donkey anti-Rabbit (1:1000, Jackson Immunoresearch). Frequency of cytoplasmic Nup62 puncta were determined by spot detection for molecule with diameter of 1 μm or larger for 39-47 cells over the course of two separate experiments.

Quantitative reverse-transcriptase polymerase chain reaction (qRT-PCR)

FG Nup knockdown validation in Drosophila Frozen fly heads (minimum of 9 flies/group) were homogenized with Trizol (Cat. No. 15596026, Ambion) within 24h of eclosion. RNA was isolated into the upper aqueous phase with chloroform addition and then precipitated out by isopropanol. RNA was then pelleted by centrifugation, washed with 75% ethanol solution and air-dried prior to

being resuspended in nuclease free water. cDNA was synthesized from equal volumes of RNA samples by iScript Select cDNA Synthesis Kit (Cat. No. 170-8897, BioRad).

In vitro transcript characterization RNA was extracted and purified from cellular samples with miRNeasy Mini Kit (Cat. No. 217004, Qiagen). cDNA was synthesized from equal volumes of RNA samples by iScript Select cDNA Synthesis Kit (Cat. No. 170-8897, BioRad).

Primers (10 μ M working concentrations) (Supplemental Table 1) were generated by Integrated DNA Technologies. qPCR reactions were prepared in SsoAdvanced Universal SYBR Green Supermix (Cat. No. 1725272, BioRad) and were run on BioRad CFX96 Real-Time System in triplicate technical replicates. Results were determined through analysis of the comparative Ct values¹⁰².

Microscopy

Image acquisition of fixed samples were acquired on a Nikon A1 laser-scanning confocal system with 40X and/or 60X oil immersion objectives (CFI Plan Fluor 40X Oil; CFI Plan Apo Lambda 60X Oil, Nikon) or Nikon N-SIM super-resolution Microscope with 60X oil immersion objectives (Plan Apo TIRF 60X Oil) and Hamamatsu C11440 Orca Flash 4.0 camera. 3D SIM images were reconstructed and then deconvolved prior to analysis. Image analysis was conducted in NIS-Elements AR Analysis 4.51.

Live-cell imaging All live-cell imaging was performed on Nikon A1 laser scanning confocal microscope outfitted with Tokai HIT stage-top incubator while utilizing 40x oil immersion objective. Stage-top incubator was allowed to equilibrate to 37 °C and 5% CO₂ for 10 min prior to imaging. HEK293 cells were transfected for 6 prior to imaging session. Images were acquired every 5 min for 15 h.

Fluorescence Recovery After Photobleaching (FRAP) Imaging FRAP studies were conduct as previously described⁹⁶. Briefly, a 60x oil immersion objective on confocal microscope was used

to monitor condensates. ROI was drawn over structure of interest and reference ROI was included in an adjacent, non-bleached cell. Four to five baseline structure images were obtained and then structure was bleached for 500 ms using 50% laser power (488nm or 594 nm laser lines). Structures were observed for 120 seconds. Data represents the fluorescence signal recovery of 11-20 structures.

Nuclear Integrity Scoring and Analysis

Following Nup62 immunostaining and imaging by structured illumination microscopy (SIM), nuclear Nup62 integrity and continuity were measured. Nuclear Nup62 integrity was scored by a blinded, unbiased observer. Nuclei that exhibited a fragmented or irregular pattern were given a lower nuclear integrity score (described in Supplemental Table 4). Furthermore, using ImageJ analysis software, we straightened the nuclear Nup62 signal and representative examples are shown above graphs (Fig 7). The profile plot was then used to measure Nup62 signal across the length (in pixels) of the select Nup62 staining. The profile plots were normalized to maximum signal intensity to account for any variability in staining intensity and also normalized to the length of measured signal to account for nuclear size variability. The area under the curve (AUC) for these profile plots was then calculated and averaged for each group (n=7-10 nuclei).

Statistical Analysis

Experimental data was collected, and outliers determined by ROUT's outlier test (Q=1%). Following removal of outliers, data sets are shown as the mean and standard error of the mean. Statistically significant differences between experimental groups were calculated by GraphPad Prism software (Version 7) and deemed significant when $p \leq 0.05$. Statistically significant differences were determined by unpaired Student's T-test when comparing two variables or one-way ANOVA with Dunnett or Tukey's multiple comparisons test when comparing multiple.

Statistical analysis of nuclear Nup62 levels in control and C9orf72 ALS iPSC neurons was conducted by two-tailed Mann-Whitney test.

Results

Nup62 is a modifier of expanded G4C2 toxicity in *Drosophila*

FG nups comprise the NPC selectivity and permeability barrier through liquid-liquid phase separation of the FG repeat domains to form a hydrogel within the NPC central channel^{86,103,104} and these are shown to exhibit neuropathological abnormalities in ALS tissue^{105–107}. However, the specific relationship between FG nups and the expanded G4C2 allele in C9-ALS/FTLD is unknown. To address this, we performed a genetic screen in the (G4C2)₃₀ expressing *Drosophila* to determine whether FG nup depletion modulates neurotoxicity associated with the rough eye phenotype (Fig 1A)^{34,94}. The GMR-Gal4 system was used to drive (G4C2)₃₀ and shRNA expression in the fly eye. Reduction of mammalian conserved FG nups through RNAi was validated through RT-qPCR (Supplemental Fig 1) and progeny rough eye phenotype was scored in a blinded manner⁹³. Expression of the (G4C2)₃₀ repeat expansion induces the rough eye phenotype when compared to control (UAS-eGFP) *Drosophila* (Fig 1B, left column)³⁴. Downregulation of specific FG nups that increased the rough eye phenotype degeneration score were classified as enhancers while those that mitigated the rough eye phenotype degeneration were suppressors (Fig 1A). Nup98 RNAi in (G4C2)₃₀ flies does not alter the rough eye phenotype (Fig 1B-C). Nup54, Nup58, or Nup153 loss suppresses the rough eye phenotype and Nup62 knockdown significantly enhances (G4C2)₃₀ mediated eye degeneration (Fig 1B-C). Importantly, RNAi mediated knockdown of FG nups alone does not alter eye phenotype in control (UAS-eGFP) *Drosophila* (Supplemental Fig 1 and Fig 1B top row). This suggests that any RNAi-mediated changes were specific to a genetic interaction with expression of the (G4C2)₃₀ transgene. These data show that specific FG nups genetically interact with the expanded G4C2 repeat and that

Nup62 may play a role in disease pathogenesis as it was a potent enhancer of eye neurodegeneration when lost.

Cellular DPR accumulation is a critical event in C9-ALS/FTLD associated neurotoxicity¹. Notably, DPRs are detected at low levels and after degeneration in the (G4C2)₃₀ repeat fly eye^{34,59}. Therefore, to validate our initial screen and determine whether DPRs might contribute to the genetic interaction seen in the (G4C2)₃₀ *Drosophila*, we also tested if Nup62 similarly enhanced the phenotype of the (G4C2)₃₆ *Drosophila* model which was previously shown to produce an abundance of DPRs (poly-GR and poly-GP)⁹⁴. Surprisingly, Nup62 loss in GMR-Gal4 (G4C2)₃₆ *Drosophila* causes robust pupal lethality and eclosion defects not observed with Nup62 knockdown alone (Fig 1D-E). Together, these data suggest that a genetic interaction likely exists between Nup62 and repeat RNA but the elevated DPR burden exacerbates the resulting *Drosophila* phenotype.

Glycine-arginine disrupts Nup62 localization *in vitro* and *in vivo*

Irregularities in nucleoporin immunostaining were previously observed in several C9-ALS/FTLD models but the direct relationship between late stage pathology (DPRs and TDP-43 inclusions) on FG nups has not been examined in depth^{59,63,88}. Our genetic screens indicate that the (G4C2)₃₆ *Drosophila* model, which accumulates DPRs, exhibits a higher sensitivity to Nup62 loss than lines with lower DPR production (Fig 1), suggesting cellular dysfunction involving Nup62 and DPRs. To validate these findings in human cells, we first assessed if DPRs disrupt nuclear Nup62 localization in HEK293 cells by expressing mCherry-tagged poly-DPR constructs expressing 50 repeats of GR, PR, GA, PA, or GP⁵⁴. Immunostaining of Nup62 and quantitative analyses of confocal projection images reveal that PR₅₀, GA₅₀, PA₅₀, and GP₅₀ do not alter nuclear Nup62 signal. However, GR₅₀ significantly reduces nuclear Nup62 intensity by 20.17% after 24 h as compared to the mCherry control (Fig 2A, Supplemental Fig 2A). Furthermore, increasing concentration of GR₅₀-plasmid DNA transfected into the cells yields a greater reduction in nuclear

Nup62 signal intensity after 24 h (Fig 2B-C) indicating a dose-dependent cellular GR₅₀ burden and nuclear Nup62 loss. Since nuclear envelope disruption is a common event during programmed cell death¹⁰⁸ and Poly-GR accumulation is cytotoxic in human cell lines and rodent models^{54,55,94,109-111}, we quantified LDH release to determine whether nuclear Nup62 signal loss was due to GR₅₀-mediated programmed cell death and no measurable difference was observed in DPR₅₀ expressing cells at the time of fixation indicating nuclear Nup62 depletion is associated with increasing cellular burden of GR (Supplemental Fig 2B). Nup62 is a short-live nucleoporin and undergoes continual turnover^{112,113}, therefore, we assessed whether GR-mediated nuclear Nup62 deficits were attributed to impairment at the transcriptional level through RT-qPCR. Consistent with previous studies in C9-ALS iPSC derived neurons⁸⁸, there was no significant difference in Nup62 mRNA levels in eGFP- and GR₅₀- transfected cells after 24 h of episomal expression indicating Nup62 defects are not due to transcription disruption (Supplemental Fig 2C). We next examined whether GR₅₀ promotes the cytoplasmic mislocalization of Nup62 protein. GR₅₀-eGFP was expressed in HEK293 cells and nuclear/cytoplasmic Nup62 signals were quantified following immunostaining and confocal imaging. GR₅₀-eGFP expression causes a modest but significant reduction in the nuclear/cytoplasmic ratio of Nup62 protein, indicating an enhanced relative cytoplasmic Nup62 signal (Fig 2D & E). Consistent with this, GR₅₀ expression produced cytoplasmic Nup62 puncta that appeared more frequently (Fig 2D & F) and with a larger area than those observed in eGFP expressing HEK293 cells (Fig 2D & G, red arrow).

Nup62 undergoes frequent turnover in both mitotic and post-mitotic neurons¹¹³⁻¹¹⁶, therefore, to ensure our findings were not limited to dividing cells, we tested whether nuclear Nup62 loss and cytoplasmic accumulation is observed in C9-ALS/FTLD patient-derived iPSC motor neurons. Differentiated control and C9-ALS/FTLD iPSC motor neuron cultures (2 control lines & 3 C9-ALS/FTLD lines; Supplemental Table 2) were assessed at 89 days post-differentiation⁶⁵ and immunostained for Nup62 and MAP2 (Fig 2H). Quantification of maximum

intensity projection confocal images revealed a 19.1% reduction in nuclear Nup62 (Fig 2I) and a 279% enrichment of cytoplasmic Nup62 (Fig 2H & J, white arrows) (Control: 1.1 vs C9-ALS/FTLD: 3.07 puncta/MAP2⁺ neuron). Notably, no significant nuclear Nup62 defects were observed in less mature iPSC neurons (28 day differentiation) from two separate C9orf72 ALS/FTLD iPSC lines and their respective isogenic controls (Supplemental Fig 2D & E). This effect is likely to be dependent upon progressive GR accumulation reported to occur over the course of 2 months in C9-ALS/FTLD iPSC neurons⁵⁶ and coincides with DPR burden driving phenotypes in *Drosophila* models with higher DPR proteins (Fig 1). Together, these data suggest cellular GR deposition causes Nup62 mislocalization from the nucleus to the cytoplasm.

To determine if GR disruption of Nup62 *in vitro* occurs *in vivo*, we quantified Nup62 localization in a newly generated transgenic poly-GR mouse model (Fig 3A-B). A GR₅₀-eGFP transgene was introduced by a Flexible Accelerated Stop Tetracycline Operator (F.A.S.T.) Cassette and driven by a ROSA26 promoter in C57BL/6 mice (Fig 3A). Immunostaining for GR₅₀-eGFP reveals its expression in tissue sections of lumbar spinal cord SMI32⁺ neurons (Fig 3B). Analyses of Nup62 localization in the GR₅₀-eGFP mouse model via immunostaining showed nuclear depletion and cytoplasmic accumulation of Nup62 protein (relative to eGFP control) in NeuN⁺ neurons of the lumbar spinal cord in 12-month-old adult animals (Fig 3C). Total cytoplasmic Nup62 droplet surface area was significantly higher in GR₅₀-eGFP mice than controls (Fig 3D). These *in vivo* data are consistent with the *in vitro* findings indicating that cellular GR accumulation promotes the nuclear loss and cytoplasmic enrichment of Nup62 protein.

Elevated Nup62 rescues C9orf72 *Drosophila*

Reduced cellular Nup62 enhances the neurotoxicity associated with expression of the G4C2-repeat expansion (Fig 1), therefore, we tested whether Nup62 overexpression is sufficient to rescue the fly eye degeneration phenotype in (G4C2)₃₆ *Drosophila*. We first generated a UAS-Nup62 expression *Drosophila* line which exhibited increased Nup62 mRNA by RT-qPCR

(Supplemental Fig 3). Nup62 *Drosophila* were crossed with the GMR-Gal4 (G4C2)₃₆ repeat expansion fly and rough eye phenotypes were then scored as a measure of neurotoxicity in the adult progeny. Nup62 expression completely abolishes the rough eye phenotype in (G4C2)₃₆ expressing *Drosophila* (Fig 4A & B), suggesting that increased Nup62 levels prevent the cytotoxic effects of expanded (G4C2)₃₆ expression *in vivo*. Since we observed Nup62 protein redistribution upon GR₅₀ cellular expression *in vitro* and *in vivo*, we next tested whether elevating Nup62 mitigates phenotypes of GR-expressing *Drosophila*. The GMR-Gal4xGR₃₆ *Drosophila* model shows a robust phenotype with reduced survival and significant retinal degeneration⁹⁴. Similarly, we observed the GMR-Gal4xGR₃₆ fly has extensive deterioration of eye size and an absence of ommatidial organization (Fig 4C). When crossed with the Nup62 *Drosophila*, there was a modest reduction in eye deterioration (Fig 4C), though this did not rescue the rough phenotype as we observed with the (G4C2)₃₆ *Drosophila* (Fig. 4A). These data provide *in vivo* evidence that C9-ALS/FTLD neurotoxicity may be attributed, in part, to Nup62 redistribution due to GR deposition, and that Nup62 expression, likely restores its localization to mitigates some of these neurotoxic effects in C9orf72 *Drosophila* models.

Poly-GR disrupts Nup62 and TDP-43 localization through stress granules

The cytoplasmic mislocalization and phosphorylation (pTDP-43) of TDP-43 is a pathological hallmark observed in the majority of ALS/FTLD patients^{4,8}. Recent neuropathological studies also show that while ~4% of TDP-43 inclusions contain GR in C9orf72 ALS/FTLD post-mortem tissue, most poly-GR accumulations colocalize with pTDP43¹¹⁷. Therefore, we next tested whether TDP-43 is altered by poly-GR expression. HEK293 cells expressing GR₅₀-eGFP resulted in the cytoplasmic mislocalization of endogenous TDP-43 as observed by immunostaining and nuclear/cytoplasmic ratio analyses (Supplemental Fig 4A & B). Interestingly, GR₅₀-eGFP-expressing cells formed droplet-like cytoplasmic condensates that colocalized with endogenous cytoplasmic TDP-43 condensates, with an average surface area of 4.90 μm^2 (Fig 5A). Analyses

of these cytoplasmic poly-GR and TDP-43 structures revealed high colocalization with a Pearson's coefficient of 0.7233 (p-value: 0.0015; Fig 5A, inset). Consistent with this, orthogonal renderings showed that cytoplasmic GR₅₀-eGFP and TDP-43 exist together within the same three-dimensional space (Fig 5A-B). Notably, this indicates that cytoplasmic GR depositions are sufficient to promote the formation of endogenous TDP-43 cytoplasmic condensates. This is supported by recent findings that show poly-GR drives aberrant phase-separation of purified or overexpressed TDP-43¹¹⁸ and these data indicate that endogenous TDP-43 similarly interacts with poly-GR inclusions *in vitro*.

Multiple cellular pathways are thought to contribute to aberrant TDP-43 phase separation and resulting pathological inclusions. Altered dynamics in membraneless organelles formed through liquid-liquid phase separation, such as SGs, are hypothesized to promote TDP-43 proteinopathy. This is supported by work showing that chronic SGs induction promotes cytoplasmic phosphorylated TDP-43 species¹¹⁹. Recent work has also identified SG-independent mechanisms that promote aberrant TDP-43 phase transitions, aggregation, and nuclear loss^{96,120,121}. Therefore, we tested whether GR-mediated sequestration of endogenous TDP-43 is associated with SG formation by immunostaining for G3BP1 and Ataxin-2 SG markers. Notably, cytoplasmic GR condensates do colocalize with G3BP1 and Ataxin-2 (Fig 5B, Supplemental Fig 4C) suggesting GR expression induces the formation of SG-like structures. GR₅₀-induction of Ataxin-2 assemblies is concentration-dependent, requiring high cellular levels of GR₅₀-eGFP to form SGs (Supplemental Fig 4C). Analysis of G3BP1 and TDP-43 in the accumulated structures revealed TDP-43 surface area is significantly less than that of G3BP1 (Fig 5C & D). Intensity profile plot analysis of Figure 5C to understand protein localization within the signal indicates that TDP-43 is localized to the GR and G3BP1 condensates (Fig 5E and Supplemental Fig 4D-E). We next characterized whether GR similarly disrupts nuclear Nup62 due to aberrant SG formation and found Nup62 to also be sequestered into these cytoplasmic GR-induced SG-like structures

along with TDP-43 and Ataxin-2 (Fig 5F, Supplemental Fig 4C, F). Notably, Nup62 consistently colocalized with SGs containing endogenous TDP-43. Profile plot analysis of cytoplasmic GR structures reveals colocalization of Nup62 within GR₅₀-eGFP:TDP-43 accumulations (Fig 5G, Supplemental Fig 4G-H). Together, this indicates that the cytoplasmic poly-GR burden directly correlates with the formation of SG-like structures in cells that recruit endogenous TDP-43 and disrupt Nup62 localization in C9orf72 ALS/FTD.

Cytoplasmic Nup62:TDP-43 interactions promote insolubility

To test the consequence of Nup62:TDP-43 cytoplasmic interactions on protein dynamics, as observed in GR-induced SGs, we generated a fluorescent mRuby-Nup62 expression plasmid that forms cytoplasmic Nup62 droplets when expressed in HEK293 cells. HEK293 cells were co-transfected with mRuby-Nup62 and eGFP-TDP43 (wild type) and 6 h after transfection, cells were monitored by longitudinal imaging for 15 h. This revealed that cytoplasmic mRuby-Nup62 condensates form with and without eGFP-TDP43 colocalization (Fig 6A). Furthermore, Nup62-mRuby forms structures that exhibit characteristics with different dynamics. Nup62-mRuby signals that did not colocalize with cytoplasmic eGFP-TDP43 exhibited characteristics of liquid-liquid phase separation in that they were dynamic, fused, and dissipated over the course of minutes (Fig 6A; “reversible”). However, when colocalized with eGFP-TDP43, mRuby-Nup62 condensates were static and formed nonspherical structures that remained present throughout the duration of the 15 h imaging session (Fig 6A, “irreversible”). We then characterized the mRuby-Nup62 signal throughout the longitudinal imaging session and found the “irreversible” structures were larger (Fig 6B), more frequently colocalized with eGFP-TDP43 (Fig 6C), and exhibited reduced circularity (Fig 6D) compared to reversible mRuby-Nup62 condensates. These features suggest that cytoplasmic Nup62 forms phase-separated liquid protein droplets that, when colocalized with cytoplasmic TDP-43, exhibit altered dynamics characteristic of gel-like or solid-state assemblies. Consistent with this, FRAP analysis of mRuby-Nup62:eGFP-TDP43 colocalized signals revealed

cytoplasmic eGFP-TDP43 (middle row) and mRuby-Nup62 (bottom row) signals do not recover after photobleaching (Fig 6E and F) indicative of insoluble protein assemblies whereas nuclear eGFP-TDP43 (top row) recovers after photobleaching, characteristic of a soluble protein. To ensure this was not an artifact of aberrant interactions driven by the Nup62 reporter orientation, we repeated this experiment with an Nup62-mRuby reporter construct and observed similar results (Supplemental Fig 5A-B). Consistent with these findings, we performed soluble/insoluble fractionation and western blot analyses of HEK293 cells co-expressing eGFP-TDP43 and mRuby-Nup62 and found that co-expression elevated insoluble eGFP-TDP43 levels (Supplemental Fig 5C-D) indicating that cytoplasmic Nup62:TDP-43 interactions promote the formation of deleterious TDP-43 phase-transitions resulting in pathological insoluble TDP-43 species. Notably, mRuby-Nup62:eGFP-TDP43 irreversible assemblies also colocalized with the nuclear import receptor, karyopherin beta 1 (KPNB1) (Supplemental Fig 5E). Since KPNB1 binds TDP-43 through its NLS, we tested if this contributes to the Nup62:TDP-43 pathological interaction. HEK293 cells co-expressing mRuby-Nup62 and eGFP-TDP43 Δ NLS (Fig 6G) showed an absence of colocalization between the two reporter proteins implicating the TDP-43 NLS is likely required for Nup62 this interaction potentially mediated by KPNB1. Together, these data show that cytoplasmic Nup62 and TDP-43 interactions, driven by the TDP-43 NLS, promote the soluble to insoluble phase of these proteins.

Cytoplasmic TDP-43 inclusions recruit Nup62 independent of stress granules

Here, we sought to test whether cytoplasmic TDP-43 assemblies similarly relocalize Nup62 absent of GR and SG induction. To achieve this, we utilized the optoTDP43 system that mimics key pathological hallmarks of the protein aggregates observed in ALS/FTLD *in vitro* and *in vivo*^{91,96,122}. The optoTDP43 construct is comprised of Cry2olig-TDP43-mCherry and photokinetic oligomerization of optoTDP43 induces its aberrant liquid-liquid phase separation upon blue-light illumination resulting in homotypic self-interactions initiated by the C-terminal low

complexity domain and later through the unbound RNA-binding domains⁹⁶. These assemblies undergo soluble-to-insoluble maturation into aggregates through aberrant liquid-liquid phase transitions independent of SGs⁹⁶. HEK293 cells were transfected with an optoTDP43 or Cry2olig-mCherry (Control) construct and exposed to blue-light for 18 h (Fig 7A). Nup62 was detected by immunofluorescent staining and N-SIM super-resolution microscopy and nuclear Nup62 signal was quantified by a blinded unbiased observer using a scoring criterion described in Supplemental Table 4. The presence of optoTDP43 inclusions correlates with a reduced nuclear Nup62 integrity score, indicating increased nuclear fragmentation and structural irregularities, as compared to Cry2olig-mCherry control cells exposed to blue-light (Fig 7B & C). Nuclear Nup62 integrity scores were complemented by profile plot analysis on nuclear Nup62 signal from Control (Cry2olig-mCherry) and OptoTDP43 cells exposed to blue-light (Fig 7D-F). Representative profile plots and corresponding images for each group in Figure 7D & E show that cells with optoTDP43 inclusions exhibited significantly reduced AUC compared to controls confirming reduced nuclear Nup62 localization (Fig 7F). Similar to GR-induced SGs, we observed optoTDP43 inclusions promoted the formation of cytoplasmic Nup62 droplets that colocalized with optoTDP43 by N-SIM super-resolution microscopy (Fig 7G, box). OptoTDP43 also colocalized with the FG nup, Nup153 (Supplemental Fig 6). We next validated if FG nups colocalize to optoTDP43 inclusions in motor neurons *in vivo* using the OK371-Gal4 optoTDP43 *Drosophila*⁹¹ and the pan-FG Nup MAb414 antibody and found that the MAb414 antibody colocalized with optoTDP43 inclusions in the ventral nerve cord of third instar larvae (Fig 7H, arrow). Interestingly, while the majority of larger optoTDP43 inclusions colocalized with FG nup staining *in vivo*, some smaller inclusions do not, suggesting cytoplasmic TDP-43 sequestration of Nup62 likely occurs as soluble cytoplasmic condensates as they mature into more insoluble inclusions through aberrant liquid-liquid phase separation (Fig 7H, asterisks). Together, these data suggest that aberrant phase separation of cytoplasmic TDP-43 condensates and pathological insoluble inclusions promote Nup62 mislocalization independent of SGs and GR deposition.

Nup62 and TDP-43 colocalize in ALS/FTLD postmortem CNS tissue.

Neuropathological analysis was then performed to determine whether Nup62 colocalized with TDP-43 proteinopathy in ALS/FTLD postmortem spinal cord, hippocampus, and cortex by immunohistochemistry (Fig 8, Supplemental Table 3). We observe a clear, uniform nuclear Nup62 signal around DAPI nuclear signal in cells without phosphorylated TDP-43 inclusions in ALS patient spinal cord (Fig 8A, asterisk). In contrast, cells with cytoplasmic and phosphorylated TDP-43 deposits exhibit a disrupted nuclear Nup62 staining (Fig 8A, arrowhead), consistent with earlier *in vitro* findings (Fig 2G). Interestingly, Nup62 was frequently observed in phospho-TDP-43⁺ inclusions in the spinal cord, cortex, and hippocampus from both C9 ALS/FTLD and sALS/FTLD patients (Fig 8B-D). This analysis of C9orf72 ALS/FTLD and sporadic ALS/FTLD suggests TDP-43 is linked with nuclear Nup62 mislocalization both *in vitro* and *in vivo*.

Although phospho-TDP-43 pathology is present in nearly all ALS cases and nearly half of FTLD cases, another RBP, FUS, is mutated in rare forms of ALS and also forms pathological inclusions in a fraction of sporadic FTLD patients^{4,5,8}. Therefore, we tested whether cytoplasmic accumulation of Nup62 is specific to TDP-43 pathology or if it is also observed in proteinopathies comprised of other RBPs, such as FUS. Immunostaining for Nup62 and FUS in two different FUS-FTLD cases did not show detectable Nup62-FUS colocalization in the hippocampus (Fig 8E). This suggests that disruption of nuclear Nup62 and its sequestration into cytoplasmic neuropathological protein inclusions is specific to the aberrant phase transitions of cytoplasmic TDP-43 in C9orf72 and sporadic ALS/FTLD.

Discussion

This study defines the pathobiological mechanisms that drive FG nup mislocalization and promote TDP-43 proteinopathy in C9orf72 and sporadic ALS/FTLD. Nucleocytoplasmic transport

dysfunction is frequently characterized in C9orf72 ALS/FTLD model systems^{59–62,65,123}. FG nups comprise the selectivity barrier of the NPC and previous reports characterized nuclear FG nup staining in C9orf72 ALS/FTLD, SOD1 ALS, and sporadic ALS/FTLD^{88,105–107}. FG nup irregularities are hypothesized to disrupt nucleocytoplasmic transport but the relationship to TDP-43 proteinopathy remains unclear. We show that Nup62, an FG nup that resides in the NPC central channel, is a potent genetic modifier of C9orf72 ALS/FTLD model systems and is aberrantly mislocalized due to cytoplasmic GR or TDP-43 through two mechanisms. In C9orf72 ALS/FTLD, GR initiates the formation of TDP-43-containing SGs that sequester nuclear Nup62 and promote its cytoplasmic redistribution. Similarly, cytoplasmic TDP-43 condensates, formed through aberrant liquid-liquid phase separation, mislocalize Nup62 into condensates that colocalize with the inclusions absent cellular GR or SGs. Furthermore, cytoplasmic Nup62:TDP-43 interactions promote soluble-to-insoluble transition of both proteins that is mediated by the TDP-43 NLS. Taken together, this study outlines a convergence of parallel upstream mechanisms involving cytoplasmic GR deposition and deleterious phase separation of cytoplasmic TDP-43 condensates that initiate FG nup mislocalization in C9orf72 and sporadic ALS/FTLD.

FG nups maintain NPC integrity^{86,104,124} and contain extensive regions of phenylalanine-glycine repeat domains. These protein domains are highly disordered and form the hydrogel-like NPC selectivity barrier through liquid-liquid phase separation^{84,103,125}. *In vivo* RNAi genetic screens performed in the (G4C2)₃₀ expressing C9orf72 ALS/FTLD *Drosophila* model identified FG nups as modifiers of the rough eye phenotype. Specifically, Nup54, Nup58, and Nup153 were suppressors, while Nup62 was an enhancer of retinal neuron degeneration (Fig 1B & C). Since Nup62 is the most potent enhancer of toxicity in the (G4C2)₃₀ *Drosophila*, we validated this finding in a second C9orf72 *Drosophila* that expresses a slightly longer (G4C2)₃₆ repeat and found that Nup62 loss results in a potent eclosion phenotype that does not occur with Nup62 RNAi alone (Fig 1D & E). We propose that this difference in phenotypes in response to Nup62 downregulation

is likely due to DPR mediated toxicity since the 36-repeat fly model produces higher levels of DPRs prior to degeneration compared to the 30-repeat fly model^{59,94}. The role of FG nups in C9-ALS/FTLD pathobiology is supported by studies in other model systems that identified some FG nups as modifiers of toxicity in (G4C2)₅₈ and (PR)₂₅ *Drosophila* models^{61,63}, and in genetic screens of (PR)₅₀- and (GR)₁₀₀- expressing yeast^{62,126}.

To address if DPRs contribute to the identified genetic interactions observed in the (G4C2)₃₆ *Drosophila*, we tested whether DPRs alter Nup62 protein in human cells. Interestingly, nuclear Nup62 localization is specifically perturbed and redistributed to the cytoplasm in response to GR expression (Fig 2D-F). Cytoplasmic Nup62 assemblies are also highly enriched (~3 fold) in C9-ALS/FTLD patient-derived iPSC neurons compared to those derived from controls (Fig 2G & I). This is also observed *in vivo* in a transgenic poly-GR expressing mouse model and expression of a codon-optimized (GR)₅₀ DPR results in loss of nuclear Nup62 signal and enrichment of cytoplasmic Nup62 droplets in lumbar spinal motor neurons (Fig. 3). This suggests poly-GR accumulation drives Nup62 mislocalization and its aberrant redistribution into cytoplasmic droplets and we hypothesize this contributes to enhanced eye phenotype in G4C2 expressing *Drosophila* upon Nup62 knockdown, since it would further reduce already low nuclear Nup62. Supportive of this, elevating Nup62 completely rescues the rough eye phenotype in (G4C2)₃₆ *Drosophila* and mitigates severe eye degeneration in a (GR)₃₆ *Drosophila* model (Fig. 4). Taken together, cytoplasmic GR accumulation promotes cytoplasmic mislocalization of Nup62 *in vitro* and *in vivo*. Notably, this is not the first study to implicate Nup62 in ALS since previous work found that its downregulation enhanced toxicity associated with poly-PR expression in *Drosophila*⁶¹ and progressive nuclear depletion of Nup62 was also characterized in the anterior horn of SOD1 G93A mice¹⁰⁶. Similarly, some fALS (SOD1 A4V) and sALS patient tissue were also found to exhibit nuclear Nup62 irregularities^{105-107,127}.

Characterization of cytoplasmic GR droplets indicate that they colocalize with endogenous TDP-43 (Fig. 5A) and G3BP1, a protein required for the assembly of SGs¹²⁸⁻¹³⁰. This finding supports work indicating that nuclear or GR promotes the spontaneous formation of SGs with abnormal dynamics, some of which contain TDP-43⁵³. Notably, the previous study did not observe cellular colocalization of GR with G3BP1 or TDP-43 proteins but did identify direct interactions between GR:G3BP1 through co-IP analyses⁵³. We found cytoplasmic GR droplets colocalize with endogenous G3BP1 and TDP-43 and this correlates with a reduction in the TDP-43 nuclear/cytoplasmic ratio in a dose-dependent manner (Fig. 5B-D, S4B-C). GR and TDP-43 signal overlap with G3BP1 with reduced TDP-43 surface area compared to G3BP1 suggesting TDP-43 lies within the SG (Fig. 5). Furthermore, cytoplasmic GR:TDP-43 assemblies colocalize with endogenous Nup62 and SG markers (Fig. 5G-F, S4F-H). Thus, high cytoplasmic GR burden promotes SG formation that recruit endogenous TDP-43 and Nup62. Previous work indicated that GR perturbs SG dynamics, thus GR:G3BP1:TDP-43:Nup62 assemblies are likely the result of pathogenic assemblies formed through aberrant liquid-liquid phase separation to promote TDP-43 aggregation⁵³. This conclusion is supported by recent work where GFP-(GR)₂₀₀ promotes the cytoplasmic mislocalization of a transiently expressed TDP-43-Myc protein *in vitro* and that (GR)₂₀ is sufficient to drive aberrant phase separation and aggregation of purified TDP-43 *in vitro*¹¹⁸. Previous studies similarly show that poly-GR colocalizes with cytoplasmic pTDP-43 inclusions in patient tissue¹¹⁷, suggesting a pathological interaction between these two proteins. AAV mediated GFP-(GR)₂₀₀ expression in rodents also resulted in cytoplasmic structures that colocalized with some nucleoporins, SG markers, and TDP-43 proteins *in vivo*¹¹⁸.

One hypothesized pathway driving deleterious TDP-43 phase separation and subsequent aggregation are through aberrant SG dynamics since chronic formation does promote TDP-43 hyperphosphorylation¹¹⁹. Notably, Nup62 was not previously reported to localize to sorbitol- and sodium arsenite-induced SGs¹³¹ as reported with GR-induced SGs here. However, recent work

in which FUS fibrils were used to induce cytoplasmic demixing of cytoplasmic TDP-43 did reveal some colocalization with Nup62 over time¹²⁰ suggesting Nup62:TDP-43 interaction may be pathogenic in nature. Therefore, we tested whether cytoplasmic Nup62 droplets, affect cytoplasmic TDP-43 condensate dynamics and solubility. Co-expressing a Nup62 reporter protein tagged with mRuby on the C- or N-terminus, and eGFP-TDP-43, resulted in cytoplasmic Nup62 droplets with two distinct characteristics determined through 15 h of live imaging. Dynamic assemblies were smaller and exhibited properties of phase separated liquid-like protein condensates and the immobile structures were angular and colocalized with eGFP-TDP-43 (Fig. 6A-D). FRAP analyses of these assemblies revealed that both Nup62 and TDP-43 do not recover from partial bleaching when colocalized suggesting this interaction promotes insolubility (Fig. 6E-F; S5A-D). KPNB1 is a nuclear transport receptor that mediates trafficking of TDP-43 via its NLS and directly interacts with FG Nups^{132,133}. We found that KPNB1 colocalized with the insoluble Nup62:TDP-43 assemblies (Fig. S5E), raising the possibility that the TDP-43 NLS contributes to the Nup62:TDP-43 interaction through KPNB1. Consistent with this, an eGFP-TDP-43 Δ NLS reporter construct does not colocalize with cytoplasmic Nup62 when co-expressed (Fig. 6G). Overall, these data suggest that cytoplasmic Nup62 droplets exhibit characteristics of proteins that undergo liquid-liquid phase separation, and it is likely that these interaction through the classical NLS promotes deleterious phase transition of cytoplasmic TDP-43 causing it to mature into insoluble inclusions.

Thus far, this work indicates that the cytoplasmic deposition of GR in C9-ALS/FTLD induces TDP-43- and Nup62- containing SGs and that cytoplasmic interaction between mislocalized Nup62 and TDP-43 promotes their insolubility. While this highlights upstream pathways that may drive FG nup defects in C9-ALS/FTLD, it does not address whether Nup62 plays a role in TDP-43 pathology absent GR in sporadic ALS/FTLD. The absence of RNA binding allows for the aberrant liquid-liquid phase separation that mature into pathological TDP-43

inclusions^{96,120}. This process can be modeled using the optoTDP43 protein to mimic end stage disease in the absence of upstream disease causing event, such as SGs or GR accumulation^{91,96,122}. Therefore, we tested if aberrant TDP-43 phase transitions in the cytoplasm similarly mislocalized Nup62 as observed with poly-GR accumulation and observed that optoTDP43 do cause fragmentation of nuclear Nup62 signal (Fig. 7 A-F). Additionally, cytoplasmic optoTDP43 inclusions, which absent of SGs, colocalize with endogenous Nup62 *in vitro* and *in vivo* (Fig. 7G-H). This suggests that cytoplasmic TDP-43 phase separation, absent of GR or SGs, promote nuclear depletion and cytoplasmic deposition of Nup62 and is consistent with work in which Nup62 is can colocalize with the C-terminal TDP-43 fragment *in vitro*¹³⁴. Notably, we did observe optoTDP43 inclusions absent Nup62 protein in the optoTDP43 *Drosophila*, raising the possibility that cytoplasmic TDP-43 phase separation may precede Nup62 sequestration (Fig 7H).

To validate physiological relevance of these findings and the relationship between TDP-43 proteinopathy and Nup62 in end stage disease, we performed immunohistological analyses in ALS and FTLN postmortem CNS tissue. Analyses of C9orf72 ALS/FTLN and sporadic ALS/FTLN samples showed robust colocalization of Nup62 with cytoplasmic pTDP-43 inclusions in patient spinal cord, cortex, and hippocampus (Fig. 8A-D). Cells that harbor Nup62:pTDP-43 inclusions also exhibit nuclear depletion of Nup62 signal in the same cell (Fig. 8A) supporting the hypothesis that aberrant TDP-43 phase transitions promote the cellular redistribution and cytoplasmic mislocalization of Nup62. Interestingly, this pathological interaction is specific to TDP-43 inclusions and not general to pathological RNA binding protein inclusions since Nup62 did not colocalize with FUS inclusions in the hippocampus of FTLN-FUS patients (Fig. 8E). Taken together, nuclear Nup62 defects and cytoplasmic mislocalization can be driven by aberrant phase transitions of cytoplasmic TDP-43 in the absence of GR accumulation.

TDP-43 inclusions are a neuropathological feature of several neurodegenerative diseases, thus, the negative impact of TDP-43 phase transitions on Nup62 maintenance may be

broadly relevant to neurodegeneration. Beyond disrupting cytoplasmic TDP-43 solubility, since Nup62 contributes to the NPC selectivity and permeability barrier, nuclear mislocalization due to cytoplasmic TDP-43 condensates may have serious implications on nucleocytoplasmic trafficking. Previous work shows nucleocytoplasmic transport impairment occurs independent of TDP-43 mislocalization in C9-ALS/FTLD iPSC neurons and this coincides with normal nuclear Nup62 integrity⁸⁸. Thus, while other pathways likely initiate transport defects observed in C9-ALS/FTLD, this is likely further exacerbated by cytoplasmic TDP-43 accumulation and Nup62:TDP-43 colocalization in late-stage disease. Furthermore, early Nup62:TDP-43 assemblies may act through a feed-forward mechanism to promote TDP-43 nuclear loss of function through a seeding event or cytoplasmic gain of function toxicity via inclusions formation. Thus, these findings suggest that NPC integrity is compromised through sequestration of Nup62 into cytoplasmic TDP-43 condensates. This process is mediated by GR-induced stress granules with perturbed dynamics in C9-ALS/FTLD or through cytoplasmic RNA deficient TDP-43 condensates in sporadic disease. Future work is required to define Nup62:TDP-43 interactions and the consequence of cytoplasmic Nup62 mislocalization on specific aspects of nucleocytoplasmic transport.

Acknowledgments

We appreciated the generosity of Akiko Takedo for sharing the Nup62 plasmid utilized in this study. This work was supported by grants from the NIH (R01NS105756 to CJD and R21NS098379 to CJD and UB, R01NS104219 to EK), the LiveLikeLou Center for ALS Research at the University of Pittsburgh Brain Institute, a fellowship and grants from Target ALS Foundation and the Frick Foundation for ALS Research, and a generous gift from Barbara McCormick to CJD. AMG was supported by the Milton Safenowitz Postdoctoral Fellowship for ALS Research of the ALS Association and NIH T32 Postdoctoral Training Fellowship Recipient (NS086749). JRM was supported by a fellowship from the Center for Protein Conformational Diseases at the University

of Pittsburgh. DT was supported by grants from MDA (#628389) and NIH R21-NS090912 . DT, BMV, and MEC were also supported by the Farber Family Foundation and the Family Strong 4 ALS foundation. JAO is an AFM-Telethon Postdoctoral Research Fellow. EK is a Les Turner ALS Research Center Investigator and a New York Stem Cell Foundation-Robertson Investigator.

References

1. Ling, S.-C., Polymenidou, M. & Cleveland, D. W. Converging mechanisms in ALS and FTD: disrupted RNA and protein homeostasis. *Neuron* 79, 416–438 (2013).
2. Lattante, S., Ciura, S., Rouleau, G. A. & Kabashi, E. Defining the genetic connection linking amyotrophic lateral sclerosis (ALS) with frontotemporal dementia (FTD). *Trends Genet.* 31, 263–273 (2015).
3. Dormann, D. & Haass, C. TDP-43 and FUS: a nuclear affair. *Trends Neurosci.* 34, 339–348 (2011).
4. Neumann, M. *et al.* Ubiquitinated TDP-43 in frontotemporal lobar degeneration and amyotrophic lateral sclerosis. *Science* 314, 130–133 (2006).
5. Neumann, M. *et al.* A new subtype of frontotemporal lobar degeneration with FUS pathology. *Brain* 132, 2922–2931 (2009).
6. Urwin, H. *et al.* FUS pathology defines the majority of tau- and TDP-43-negative frontotemporal lobar degeneration. *Acta Neuropathol.* 120, 33–41 (2010).
7. Kwiatkowski, T. J. *et al.* Mutations in the FUS/TLS gene on chromosome 16 cause familial amyotrophic lateral sclerosis. *Science* 323, 1205–1208 (2009).
8. Arai, T. *et al.* TDP-43 is a component of ubiquitin-positive tau-negative inclusions in frontotemporal lobar degeneration and amyotrophic lateral sclerosis. *Biochem. Biophys. Res. Commun.* 351, 602–611 (2006).
9. Vance, C. *et al.* Mutations in FUS, an RNA processing protein, cause familial amyotrophic lateral sclerosis type 6. *Science* 323, 1208–1211 (2009).
10. DeJesus-Hernandez, M. *et al.* Expanded GGGGCC hexanucleotide repeat in noncoding region of C9ORF72 causes chromosome 9p-linked FTD and ALS. *Neuron* 72, 245–256 (2011).
11. Nguyen, H. P., Van Broeckhoven, C. & van der Zee, J. ALS Genes in the Genomic Era and their Implications for FTD. *Trends Genet.* 34, 404–423 (2018).
12. Renton, A. E. *et al.* A hexanucleotide repeat expansion in C9ORF72 is the cause of chromosome 9p21-linked ALS-FTD. *Neuron* 72, 257–268 (2011).
13. Rademakers, R. C9orf72 repeat expansions in patients with ALS and FTD. *Lancet Neurol.* 11, 297–298 (2012).
14. Ciura, S. *et al.* Loss of function of C9orf72 causes motor deficits in a zebrafish model of amyotrophic lateral sclerosis. *Ann. Neurol.* 74, 180–187 (2013).
15. Donnelly, C. J. *et al.* RNA toxicity from the ALS/FTD C9ORF72 expansion is mitigated by antisense intervention. *Neuron* 80, 415–428 (2013).
16. Almeida, S. *et al.* Modeling key pathological features of frontotemporal dementia with C9ORF72 repeat expansion in iPSC-derived human neurons. *Acta Neuropathol.* 126, 385–399 (2013).

17. Shi, Y. *et al.* Haploinsufficiency leads to neurodegeneration in C9ORF72 ALS/FTD human induced motor neurons. *Nat. Med.* 24, 313–325 (2018).
18. Belzil, V. V. *et al.* Reduced C9orf72 gene expression in c9FTD/ALS is caused by histone trimethylation, an epigenetic event detectable in blood. *Acta Neuropathol.* 126, 895–905 (2013).
19. van Blitterswijk, M. *et al.* Novel clinical associations with specific C9ORF72 transcripts in patients with repeat expansions in C9ORF72. *Acta Neuropathol.* 130, 863–876 (2015).
20. Balendra, R. & Isaacs, A. M. C9orf72-mediated ALS and FTD: multiple pathways to disease. *Nat. Rev. Neurol.* 14, 544–558 (2018).
21. Koppers, M. *et al.* C9orf72 ablation in mice does not cause motor neuron degeneration or motor deficits. *Ann. Neurol.* 78, 426–438 (2015).
22. O'Rourke, J. G. *et al.* C9orf72 is required for proper macrophage and microglial function in mice. *Science* 351, 1324–1329 (2016).
23. Jiang, J. *et al.* Gain of Toxicity from ALS/FTD-Linked Repeat Expansions in C9ORF72 Is Alleviated by Antisense Oligonucleotides Targeting GGGGCC-Containing RNAs. *Neuron* 90, 535–550 (2016).
24. Atanasio, A. *et al.* C9orf72 ablation causes immune dysregulation characterized by leukocyte expansion, autoantibody production, and glomerulonephropathy in mice. *Sci. Rep.* 6, 23204 (2016).
25. Hautbergue, G. M. *et al.* SRSF1-dependent nuclear export inhibition of C9ORF72 repeat transcripts prevents neurodegeneration and associated motor deficits. *Nat. Commun.* 8, 16063 (2017).
26. Stopford, M. J. *et al.* C9ORF72 hexanucleotide repeat exerts toxicity in a stable, inducible motor neuronal cell model, which is rescued by partial depletion of Pten. *Hum. Mol. Genet.* 26, 1133–1145 (2017).
27. Batra, R. & Lee, C. W. Mouse models of c9orf72 hexanucleotide repeat expansion in amyotrophic lateral sclerosis/ frontotemporal dementia. *Front. Cell Neurosci.* 11, 196 (2017).
28. Chew, J. *et al.* Neurodegeneration. C9ORF72 repeat expansions in mice cause TDP-43 pathology, neuronal loss, and behavioral deficits. *Science* 348, 1151–1154 (2015).
29. Liu, Y. *et al.* C9orf72 BAC Mouse Model with Motor Deficits and Neurodegenerative Features of ALS/FTD. *Neuron* 90, 521–534 (2016).
30. O'Rourke, J. G. *et al.* C9orf72 BAC transgenic mice display typical pathologic features of ALS/FTD. *Neuron* 88, 892–901 (2015).
31. Zhu, Q. *et al.* Reduced C9ORF72 function exacerbates gain of toxicity from ALS/FTD-causing repeat expansion in C9orf72. *Nat. Neurosci.* 23, 615–624 (2020).
32. Shao, Q. *et al.* C9orf72 deficiency promotes motor deficits of a C9ALS/FTD mouse model in a dose-dependent manner. *Acta Neuropathol. Commun.* 7, 32 (2019).

33. Cooper-Knock, J. *et al.* Sequestration of multiple RNA recognition motif-containing proteins by C9orf72 repeat expansions. *Brain* 137, 2040–2051 (2014).
34. Xu, Z. *et al.* Expanded GGGGCC repeat RNA associated with amyotrophic lateral sclerosis and frontotemporal dementia causes neurodegeneration. *Proc. Natl. Acad. Sci. USA* 110, 7778–7783 (2013).
35. Haeusler, A. R. *et al.* C9orf72 nucleotide repeat structures initiate molecular cascades of disease. *Nature* 507, 195–200 (2014).
36. Conlon, E. G. *et al.* The C9ORF72 GGGGCC expansion forms RNA G-quadruplex inclusions and sequesters hnRNP H to disrupt splicing in ALS brains. *Elife* 5, (2016).
37. Mori, K. *et al.* hnRNP A3 binds to GGGGCC repeats and is a constituent of p62-positive/TDP43-negative inclusions in the hippocampus of patients with C9orf72 mutations. *Acta Neuropathol.* 125, 413–423 (2013).
38. Celona, B. *et al.* Suppression of C9orf72 RNA repeat-induced neurotoxicity by the ALS-associated RNA-binding protein Zfp106. *Elife* 6, (2017).
39. Freibaum, B. D. & Taylor, J. P. The Role of Dipeptide Repeats in C9ORF72-Related ALS-FTD. *Front. Mol. Neurosci.* 10, 35 (2017).
40. Cleary, J. D. & Ranum, L. P. New developments in RAN translation: insights from multiple diseases. *Curr. Opin. Genet. Dev.* 44, 125–134 (2017).
41. Zu, T. *et al.* Non-ATG-initiated translation directed by microsatellite expansions. *Proc. Natl. Acad. Sci. USA* 108, 260–265 (2011).
42. Mori, K. *et al.* Bidirectional transcripts of the expanded C9orf72 hexanucleotide repeat are translated into aggregating dipeptide repeat proteins. *Acta Neuropathol.* 126, 881–893 (2013).
43. Mori, K. *et al.* The C9orf72 GGGGCC repeat is translated into aggregating dipeptide-repeat proteins in FTLD/ALS. *Science* 339, 1335–1338 (2013).
44. Ash, P. E. A. *et al.* Unconventional translation of C9ORF72 GGGGCC expansion generates insoluble polypeptides specific to c9FTD/ALS. *Neuron* 77, 639–646 (2013).
45. Gendron, T. F. *et al.* Antisense transcripts of the expanded C9ORF72 hexanucleotide repeat form nuclear RNA foci and undergo repeat-associated non-ATG translation in c9FTD/ALS. *Acta Neuropathol.* 126, 829–844 (2013).
46. Sareen, D. *et al.* Targeting RNA foci in iPSC-derived motor neurons from ALS patients with a C9ORF72 repeat expansion. *Sci. Transl. Med.* 5, 208ra149 (2013).
47. Cooper-Knock, J. *et al.* Antisense RNA foci in the motor neurons of C9ORF72-ALS patients are associated with TDP-43 proteinopathy. *Acta Neuropathol.* 130, 63–75 (2015).
48. Mizielińska, S. *et al.* C9orf72 frontotemporal lobar degeneration is characterised by frequent neuronal sense and antisense RNA foci. *Acta Neuropathol.* 126, 845–857 (2013).
49. White, M. R. *et al.* C9orf72 poly(pr) dipeptide repeats disturb biomolecular phase separation and disrupt nucleolar function. *Mol. Cell* 74, 713–728.e6 (2019).

50. Xu, W. & Xu, J. C9orf72 Dipeptide Repeats Cause Selective Neurodegeneration and Cell-Autonomous Excitotoxicity in *Drosophila* Glutamatergic Neurons. *J. Neurosci.* 38, 7741–7752 (2018).
51. Starr, A. & Sattler, R. Synaptic dysfunction and altered excitability in C9ORF72 ALS/FTD. *Brain Res.* 1693, 98–108 (2018).
52. Boeynaems, S. *et al.* Phase separation of c9orf72 dipeptide repeats perturbs stress granule dynamics. *Mol. Cell* 65, 1044–1055.e5 (2017).
53. Lee, K.-H. *et al.* C9orf72 Dipeptide Repeats Impair the Assembly, Dynamics, and Function of Membrane-Less Organelles. *Cell* 167, 774–788.e17 (2016).
54. Wen, X. *et al.* Antisense proline-arginine RAN dipeptides linked to C9ORF72-ALS/FTD form toxic nuclear aggregates that initiate in vitro and in vivo neuronal death. *Neuron* 84, 1213–1225 (2014).
55. Zhang, Y.-J. *et al.* Poly(GR) impairs protein translation and stress granule dynamics in C9orf72-associated frontotemporal dementia and amyotrophic lateral sclerosis. *Nat. Med.* 24, 1136–1142 (2018).
56. Lopez-Gonzalez, R. *et al.* Poly(GR) in C9ORF72-Related ALS/FTD Compromises Mitochondrial Function and Increases Oxidative Stress and DNA Damage in iPSC-Derived Motor Neurons. *Neuron* 92, 383–391 (2016).
57. Choi, S. Y. *et al.* C9ORF72-ALS/FTD-associated poly(GR) binds Atp5a1 and compromises mitochondrial function in vivo. *Nat. Neurosci.* 22, 851–862 (2019).
58. Hartmann, H. *et al.* Proteomics and C9orf72 neuropathology identify ribosomes as poly-GR/PR interactors driving toxicity. *Life Sci. Alliance* 1, e201800070 (2018).
59. Zhang, K. *et al.* The C9orf72 repeat expansion disrupts nucleocytoplasmic transport. *Nature* 525, 56–61 (2015).
60. Hayes, L. R., Duan, L., Bowen, K., Kalab, P. & Rothstein, J. D. C9orf72 arginine-rich dipeptide repeat proteins disrupt karyopherin-mediated nuclear import. *Elife* 9, (2020).
61. Boeynaems, S. *et al.* *Drosophila* screen connects nuclear transport genes to DPR pathology in c9ALS/FTD. *Sci. Rep.* 6, 20877 (2016).
62. Jovičić, A. *et al.* Modifiers of C9orf72 dipeptide repeat toxicity connect nucleocytoplasmic transport defects to FTD/ALS. *Nat. Neurosci.* 18, 1226–1229 (2015).
63. Freibaum, B. D. *et al.* GGGGCC repeat expansion in C9orf72 compromises nucleocytoplasmic transport. *Nature* 525, 129–133 (2015).
64. Shi, K. Y. *et al.* Toxic PR_n poly-dipeptides encoded by the C9orf72 repeat expansion block nuclear import and export. *Proc. Natl. Acad. Sci. USA* 114, E1111–E1117 (2017).
65. Ortega, J. A. *et al.* Nucleocytoplasmic Proteomic Analysis Uncovers eRF1 and Nonsense-Mediated Decay as Modifiers of ALS/FTD C9orf72 Toxicity. *Neuron* 106, 90–107.e13 (2020).

66. Hutten, S. *et al.* Nuclear Import Receptors Directly Bind to Arginine-Rich Dipeptide Repeat Proteins and Suppress Their Pathological Interactions. *Cell Rep.* 33, 108538 (2020).
67. Görlich, D. & Mattaj, I. W. Nucleocytoplasmic transport. *Science* 271, 1513–1518 (1996).
68. Cronshaw, J. M., Krutchinsky, A. N., Zhang, W., Chait, B. T. & Matunis, M. J. Proteomic analysis of the mammalian nuclear pore complex. *J. Cell Biol.* 158, 915–927 (2002).
69. Patel, S. S., Belmont, B. J., Sante, J. M. & Rexach, M. F. Natively unfolded nucleoporins gate protein diffusion across the nuclear pore complex. *Cell* 129, 83–96 (2007).
70. Ribbeck, K. & Görlich, D. The permeability barrier of nuclear pore complexes appears to operate via hydrophobic exclusion. *EMBO J.* 21, 2664–2671 (2002).
71. Ribbeck, K. & Görlich, D. Kinetic analysis of translocation through nuclear pore complexes. *EMBO J.* 20, 1320–1330 (2001).
72. Mohr, D., Frey, S., Fischer, T., Güttler, T. & Görlich, D. Characterisation of the passive permeability barrier of nuclear pore complexes. *EMBO J.* 28, 2541–2553 (2009).
73. Bischoff, F. R., Krebber, H., Kempf, T., Hermes, I. & Ponstingl, H. Human RanGTPase-activating protein RanGAP1 is a homologue of yeast Rna1p involved in mRNA processing and transport. *Proc. Natl. Acad. Sci. USA* 92, 1749–1753 (1995).
74. Kusano, A., Staber, C. & Ganetzky, B. Nuclear mislocalization of enzymatically active RanGAP causes segregation distortion in *Drosophila*. *Dev. Cell* 1, 351–361 (2001).
75. Bischoff, F. R., Klebe, C., Kretschmer, J., Wittinghofer, A. & Ponstingl, H. RanGAP1 induces GTPase activity of nuclear Ras-related Ran. *Proc. Natl. Acad. Sci. USA* 91, 2587–2591 (1994).
76. Steggerda, S. M. & Paschal, B. M. Regulation of nuclear import and export by the GTPase Ran. *Int Rev Cytol* 217, 41–91 (2002).
77. Macara, I. G. Transport into and out of the Nucleus. *Microbiol. Mol. Biol. Rev.* 65, 570–594 (2001).
78. Wenthe, S. R. & Rout, M. P. The nuclear pore complex and nuclear transport. *Cold Spring Harb. Perspect. Biol.* 2, a000562 (2010).
79. Aramburu, I. V. & Lemke, E. A. Floppy but not sloppy: Interaction mechanism of FG-nucleoporins and nuclear transport receptors. *Semin. Cell Dev. Biol.* 68, 34–41 (2017).
80. Kapinos, L. E., Huang, B., Rencurel, C. & Lim, R. Y. H. Karyopherins regulate nuclear pore complex barrier and transport function. *J. Cell Biol.* 216, 3609–3624 (2017).
81. Allen, N. P., Huang, L., Burlingame, A. & Rexach, M. Proteomic analysis of nucleoporin interacting proteins. *J. Biol. Chem.* 276, 29268–29274 (2001).
82. Rexach, M. & Blobel, G. Protein import into nuclei: association and dissociation reactions involving transport substrate, transport factors, and nucleoporins. *Cell* 83, 683–692 (1995).

83. Kim, S. J. *et al.* Integrative structure and functional anatomy of a nuclear pore complex. *Nature* 555, 475–482 (2018).
84. Frey, S. & Görlich, D. A saturated FG-repeat hydrogel can reproduce the permeability properties of nuclear pore complexes. *Cell* 130, 512–523 (2007).
85. Denning, D. P., Patel, S. S., Uversky, V., Fink, A. L. & Rexach, M. Disorder in the nuclear pore complex: the FG repeat regions of nucleoporins are natively unfolded. *Proc. Natl. Acad. Sci. USA* 100, 2450–2455 (2003).
86. Labokha, A. A. *et al.* Systematic analysis of barrier-forming FG hydrogels from *Xenopus* nuclear pore complexes. *EMBO J.* 32, 204–218 (2013).
87. Solomon, D. A. *et al.* A feedback loop between dipeptide-repeat protein, TDP-43 and karyopherin- α mediates C9orf72-related neurodegeneration. *Brain* 141, 2908–2924 (2018).
88. Coyne, A. N. *et al.* G4C2 Repeat RNA Initiates a POM121-Mediated Reduction in Specific Nucleoporins in C9orf72 ALS/FTD. *Neuron* (2020). doi:10.1016/j.neuron.2020.06.027
89. Ni, J.-Q. *et al.* A genome-scale shRNA resource for transgenic RNAi in *Drosophila*. *Nat. Methods* 8, 405–407 (2011).
90. Casci, I. *et al.* Muscleblind acts as a modifier of FUS toxicity by modulating stress granule dynamics and SMN localization. *Nat. Commun.* 10, 5583 (2019).
91. Otte, C. G. *et al.* Optogenetic TDP-43 nucleation induces persistent insoluble species and progressive motor dysfunction in vivo. *Neurobiol. Dis.* 146, 105078 (2020).
92. Ramesh, N., Kour, S., Anderson, E. N., Rajasundaram, D. & Pandey, U. B. RNA-recognition motif in Matrin-3 mediates neurodegeneration through interaction with hnRNPM. *Acta Neuropathol. Commun.* 8, 138 (2020).
93. Pandey, U. B. *et al.* HDAC6 rescues neurodegeneration and provides an essential link between autophagy and the UPS. *Nature* 447, 859–863 (2007).
94. Mizielińska, S. *et al.* C9orf72 repeat expansions cause neurodegeneration in *Drosophila* through arginine-rich proteins. *Science* 345, 1192–1194 (2014).
95. Ziller, M. J. *et al.* Dissecting the functional consequences of de novo DNA methylation dynamics in human motor neuron differentiation and physiology. *Cell Stem Cell* 22, 559–574.e9 (2018).
96. Mann, J. R. *et al.* RNA Binding Antagonizes Neurotoxic Phase Transitions of TDP-43. *Neuron* 102, 321–338.e8 (2019).
97. Tanaka, K. F. *et al.* Flexible Accelerated STOP Tetracycline Operator-knockin (FAST): a versatile and efficient new gene modulating system. *Biol. Psychiatry* 67, 770–773 (2010).
98. Kisseberth, W. C., Brettingen, N. T., Lohse, J. K. & Sandgren, E. P. Ubiquitous expression of marker transgenes in mice and rats. *Dev. Biol.* 214, 128–138 (1999).
99. Soriano, P. Generalized lacZ expression with the ROSA26 Cre reporter strain. *Nat. Genet.* 21, 70–71 (1999).

100. Zambrowicz, B. P. *et al.* Disruption of overlapping transcripts in the ROSA beta geo 26 gene trap strain leads to widespread expression of beta-galactosidase in mouse embryos and hematopoietic cells. *Proc. Natl. Acad. Sci. USA* 94, 3789–3794 (1997).
101. Kinoshita, Y. *et al.* Role for NUP62 depletion and PYK2 redistribution in dendritic retraction resulting from chronic stress. *Proc. Natl. Acad. Sci. USA* 111, 16130–16135 (2014).
102. Schmittgen, T. D. & Livak, K. J. Analyzing real-time PCR data by the comparative C(T) method. *Nat. Protoc.* 3, 1101–1108 (2008).
103. Celetti, G. *et al.* The liquid state of FG-nucleoporins mimics permeability barrier properties of nuclear pore complexes. *J. Cell Biol.* 219, (2020).
104. Li, C., Goryaynov, A. & Yang, W. The selective permeability barrier in the nuclear pore complex. *Nucleus* 7, 430–446 (2016).
105. Aizawa, H., Yamashita, T., Kato, H., Kimura, T. & Kwak, S. Impaired Nucleoporins Are Present in Sporadic Amyotrophic Lateral Sclerosis Motor Neurons that Exhibit Mislocalization of the 43-kDa TAR DNA-Binding Protein. *J. Clin. Neurol.* 15, 62–67 (2019).
106. Kinoshita, Y. *et al.* Nuclear contour irregularity and abnormal transporter protein distribution in anterior horn cells in amyotrophic lateral sclerosis. *J. Neuropathol. Exp. Neurol.* 68, 1184–1192 (2009).
107. Yamashita, T., Aizawa, H., Teramoto, S., Akamatsu, M. & Kwak, S. Calpain-dependent disruption of nucleo-cytoplasmic transport in ALS motor neurons. *Sci. Rep.* 7, 39994 (2017).
108. Wu, J. *et al.* Caspase-mediated cleavage of C53/LZAP protein causes abnormal microtubule bundling and rupture of the nuclear envelope. *Cell Res.* 23, 691–704 (2013).
109. Yamakawa, M. *et al.* Characterization of the dipeptide repeat protein in the molecular pathogenesis of c9FTD/ALS. *Hum. Mol. Genet.* 24, 1630–1645 (2015).
110. Sakae, N. *et al.* Poly-GR dipeptide repeat polymers correlate with neurodegeneration and Clinicopathological subtypes in C9ORF72-related brain disease. *Acta Neuropathol. Commun.* 6, 63 (2018).
111. Kramer, N. J. *et al.* CRISPR-Cas9 screens in human cells and primary neurons identify modifiers of C9ORF72 dipeptide-repeat-protein toxicity. *Nat. Genet.* 50, 603–612 (2018).
112. Toyama, B. H. *et al.* Identification of long-lived proteins reveals exceptional stability of essential cellular structures. *Cell* 154, 971–982 (2013).
113. D'Angelo, M. A., Raices, M., Panowski, S. H. & Hetzer, M. W. Age-dependent deterioration of nuclear pore complexes causes a loss of nuclear integrity in postmitotic cells. *Cell* 136, 284–295 (2009).
114. Otsuka, S. & Ellenberg, J. Mechanisms of nuclear pore complex assembly - two different ways of building one molecular machine. *FEBS Lett.* 592, 475–488 (2018).

115. Hetzer, M. W. The role of the nuclear pore complex in aging of post-mitotic cells. *Aging (Albany, NY)* 2, 74–75 (2010).
116. Dörrbaum, A. R., Kochen, L., Langer, J. D. & Schuman, E. M. Local and global influences on protein turnover in neurons and glia. *Elife* 7, (2018).
117. Saberi, S. *et al.* Sense-encoded poly-GR dipeptide repeat proteins correlate to neurodegeneration and uniquely co-localize with TDP-43 in dendrites of repeat-expanded C9orf72 amyotrophic lateral sclerosis. *Acta Neuropathol.* 135, 459–474 (2018).
118. Cook, C. N. *et al.* C9orf72 poly(GR) aggregation induces TDP-43 proteinopathy. *Sci. Transl. Med.* 12, (2020).
119. McGurk, L. *et al.* Poly(ADP-Ribose) Prevents Pathological Phase Separation of TDP-43 by Promoting Liquid Demixing and Stress Granule Localization. *Mol. Cell* 71, 703–717.e9 (2018).
120. Gasset-Rosa, F. *et al.* Cytoplasmic TDP-43 De-mixing Independent of Stress Granules Drives Inhibition of Nuclear Import, Loss of Nuclear TDP-43, and Cell Death. *Neuron* 102, 339–357.e7 (2019).
121. Chen, Y. & Cohen, T. J. Aggregation of the nucleic acid-binding protein TDP-43 occurs via distinct routes that are coordinated with stress granule formation. *J. Biol. Chem.* 294, 3696–3706 (2019).
122. Asakawa, K., Handa, H. & Kawakami, K. Optogenetic modulation of TDP-43 oligomerization accelerates ALS-related pathologies in the spinal motor neurons. *Nat. Commun.* 11, 1004 (2020).
123. Kim, H. J. & Taylor, J. P. Lost in transportation: nucleocytoplasmic transport defects in ALS and other neurodegenerative diseases. *Neuron* 96, 285–297 (2017).
124. Terry, L. J. & Wente, S. R. Flexible gates: dynamic topologies and functions for FG nucleoporins in nucleocytoplasmic transport. *Eukaryotic Cell* 8, 1814–1827 (2009).
125. Ader, C. *et al.* Amyloid-like interactions within nucleoporin FG hydrogels. *Proc. Natl. Acad. Sci. USA* 107, 6281–6285 (2010).
126. Chai, N. & Gitler, A. D. Yeast screen for modifiers of C9orf72 poly(glycine-arginine) dipeptide repeat toxicity. *FEMS Yeast Res* 18, (2018).
127. Nagara, Y. *et al.* Impaired cytoplasmic-nuclear transport of hypoxia-inducible factor-1 α in amyotrophic lateral sclerosis. *Brain Pathol.* 23, 534–546 (2013).
128. Yang, P. *et al.* G3BP1 Is a Tunable Switch that Triggers Phase Separation to Assemble Stress Granules. *Cell* 181, 325–345.e28 (2020).
129. Kedersha, N. *et al.* G3BP-Caprin1-USP10 complexes mediate stress granule condensation and associate with 40S subunits. *J. Cell Biol.* 212, 845–860 (2016).
130. Bracha, D. *et al.* Mapping local and global liquid phase behavior in living cells using photo-oligomerizable seeds. *Cell* 175, 1467–1480.e13 (2018).

131. Zhang, K. *et al.* Stress granule assembly disrupts nucleocytoplasmic transport. *Cell* 173, 958–971.e17 (2018).
132. Ben-Efraim, I. & Gerace, L. Gradient of increasing affinity of importin beta for nucleoporins along the pathway of nuclear import. *J. Cell Biol.* 152, 411–417 (2001).
133. Walther, T. C. *et al.* RanGTP mediates nuclear pore complex assembly. *Nature* 424, 689–694 (2003).
134. Chou, C.-C. *et al.* TDP-43 pathology disrupts nuclear pore complexes and nucleocytoplasmic transport in ALS/FTD. *Nat. Neurosci.* 21, 228–239 (2018).

Figure 1

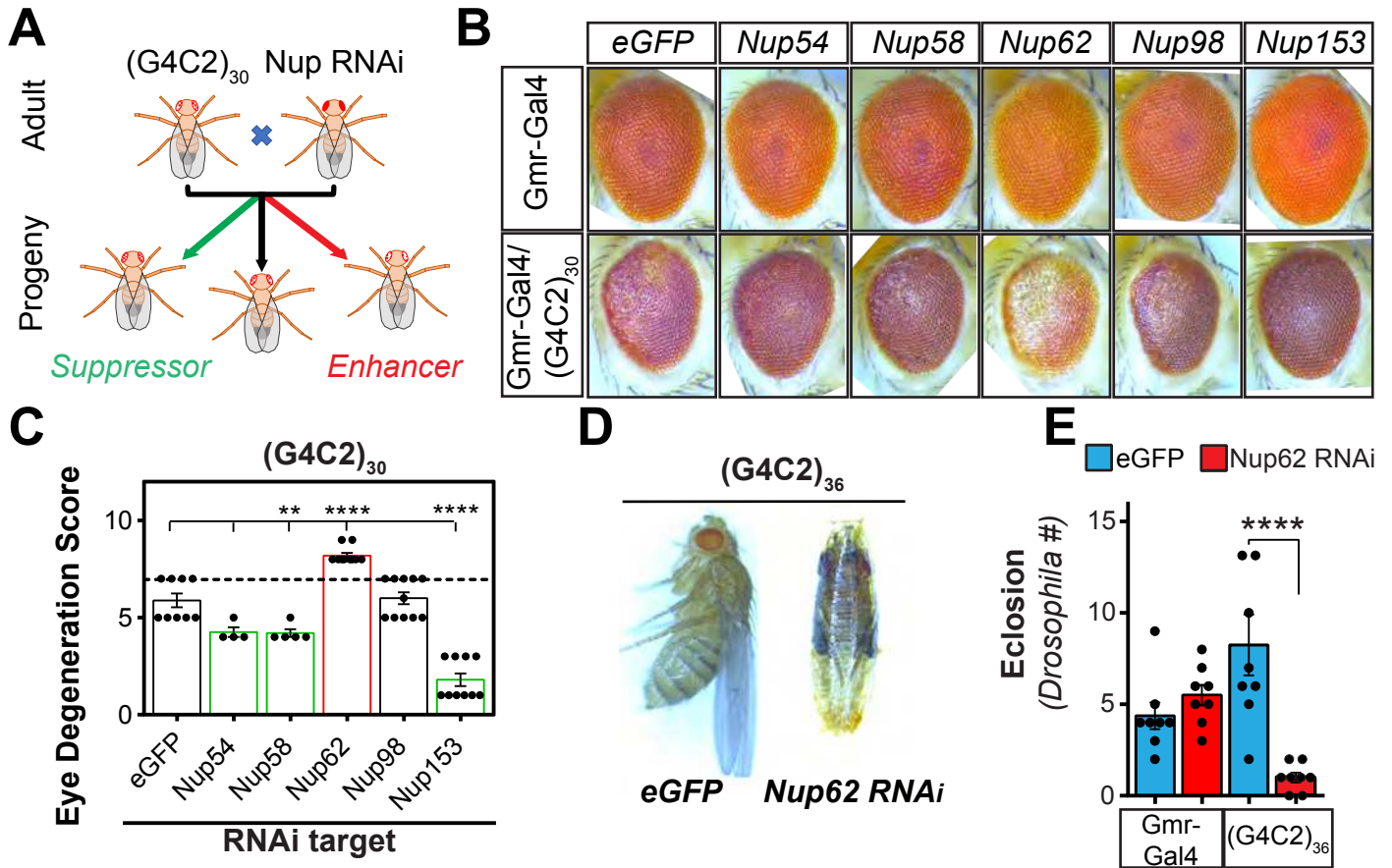


Figure 1: FG Nucleoporins are genetic modifiers of the G4C2 repeat expansion in *Drosophila*.

A) Schematic describing the methods used to identify genetic modifiers of G4C2 repeat expansion-mediated degeneration. A reduction in G4C2 repeat expansion fly eye degeneration Nup RNAi is classified as a genetic suppressor while increases are identified as genetic enhancers.

B) Representative images of fly eyes from GMR-Gal4 wild-type (top row) or (G4C2)₃₀ repeat expansion (bottom row) flies combined with control or UAS-Nup RNAi flies.

C) Quantification of scored fly eye degeneration. Unchanged degeneration score is shown by black bars while genetic modifiers that increase eye degeneration are in red (enhancer) or reduce eye degeneration are in green (suppressor) eye degeneration relative to (G4C2)₃₀ repeat expansion + eGFP control. The dashed horizontal line indicates the score for (G4C2)₃₀ repeat expansion eye degeneration alone.

D) Combination GMR-Gal4; (G4C2)₃₆ repeat expansion were crossed with a UAS-Nup62 RNAi or UAS-eGFP fly. Shown are representative images of these flies 0-1 day post eclosion.

E) Bar graph shows the quantification for (G4C2)₃₆ repeat expansion fly eclosion in the presence and absence of Nup62 RNAi. The bars show average eclosion over the course of eight days while individual dots are representative of fly counts for one 24 h eclosion period. (G4C2)₃₆;GMR-GAL4 line crossed with UAS-EGFP fly line was used as the control group. Statistically significant differences in fly eye degeneration was determined by one-way ANOVA with Tukey's multiple comparison's test: ** $p \leq 0.01$; **** $p \leq 0.0001$ vs control. Statistically significant differences in eclosion frequency was determined by one-way ANOVA with Dunnett's multiple comparison's test: **** $p \leq 0.0001$ vs UAS-EGFP x (G4C2)₃₆ repeat expansion fly.

Figure 2

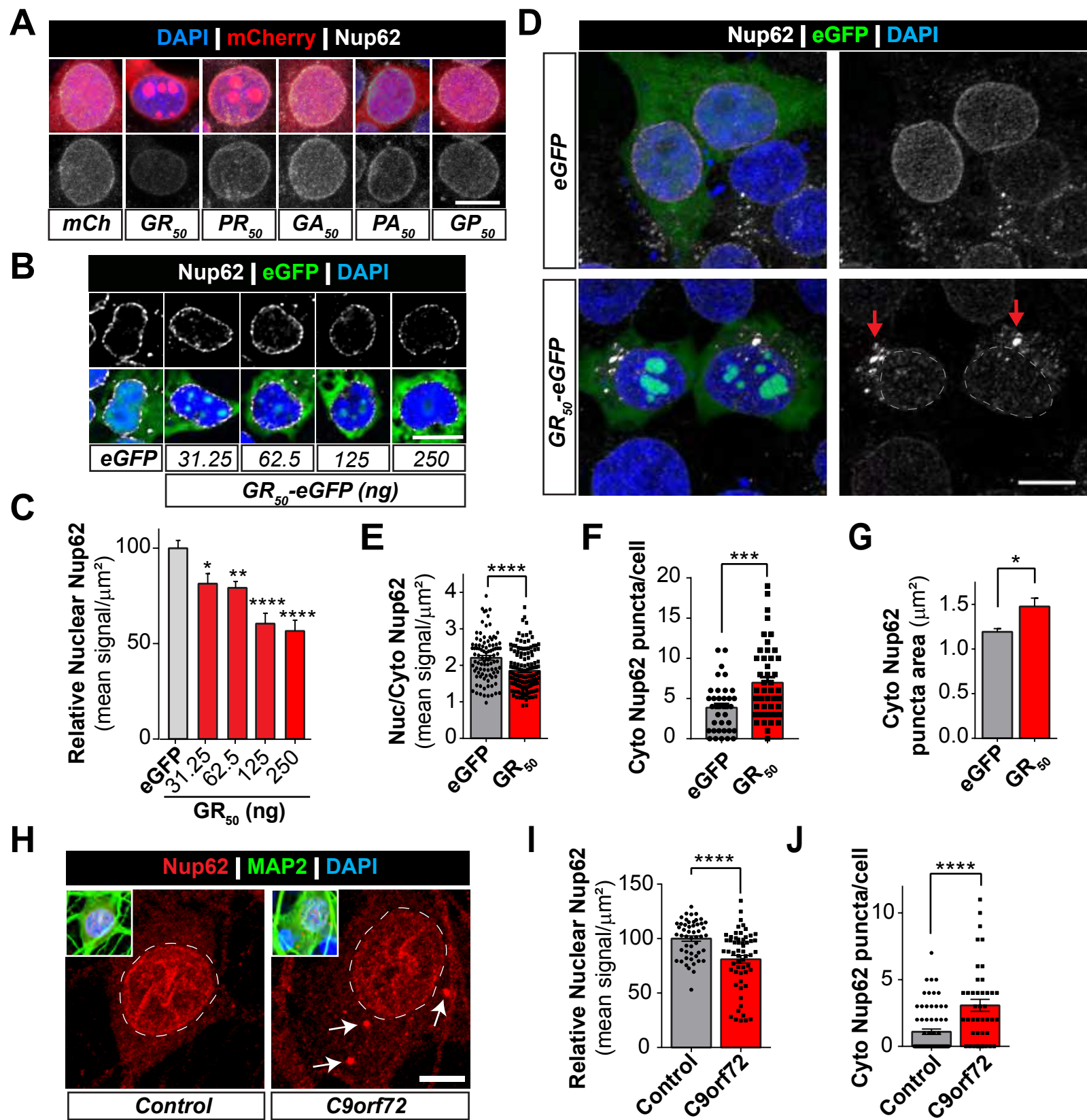


Figure 2. Poly-GR alters Nup62 localization *in vitro*.

A) Nuclear Nup62 (white) levels were assessed in HEK293 cells expressing mCherry-tagged poly-DPR constructs (red) by immunofluorescent staining and confocal microscopy. Representative maximum intensity projection images are shown. Nuclear Nup62 quantification is shown in Supplemental Fig 2A.

B) HEK293 cells were transfected with increasing amounts of GR50-eGFP plasmid DNA and immunostained for Nup62. Images were processed by automatic deconvolution in Nikon Elements. Single slice images (0.2 μm) of Nup62 (white) show dose-dependent reduction in nuclear Nup62 with increasing GR50-eGFP plasmid DNA. Scale bar: 20 μm

C) Nuclear Nup62 signal was quantified in maximum intensity projection confocal images following immunofluorescent staining (n=47-93 cells/group). Data corresponds to images presented in Fig 2B.

D) To assess whether GR50-eGFP alters nuclear Nup62 localization, HEK293 cells were transfected with eGFP (Control) or GR50-eGFP (green) and immunostained for Nup62 (white). Representative confocal images show nuclear Nup62 depletion that coincides with cytoplasmic Nup62 puncta accumulation. Nuclear compartment is highlighted by dashed white line and cytoplasmic Nup62 accumulations are indicated by red arrow.

E) Quantification of nuclear/cytoplasmic distribution of Nup62 signal corresponding to Fig 2D representative images. Regions of interest (ROIs) were drawn around DAPI or cytoplasm signals to determine Nup62 in the respective regions. The distribution for each cell was determined and then averaged for n=96-138 cells across four independent experiments.

F) We identified cytoplasmic Nup62 puncta by spot detection (diameter 1 μm or larger) methods and counted the frequency of these structures in each HEK293 cell (n=39-47 cells). Quantification reveals an increased cytoplasmic Nup62 prevalence due to GR₅₀ expression.

G) Cytoplasmic Nup62 puncta were detected by ROI automatic detection and quantification reveals GR50-eGFP causes a significant increase in their size relative to eGFP control.

H) Nup62 immunostaining (red) is shown in the representative confocal maximum intensity projection images of healthy control and C9-ALS MAP2⁺ iPSC neurons that had been matured and differentiated for 89 days. DAPI⁺ nuclear compartment is highlighted with dashed white line and cytoplasmic Nup62 puncta are indicated by white arrows.

I) The number of Nup62 puncta in MAP2⁺ iPSC neurons is quantified from confocal images represented in Figure 2G. Data analysis reveals an increase in cytoplasmic Nup62 puncta quantity in C9orf72 iPSC neurons. Average cytoplasmic Nup62 puncta per cell are shown by the graph bars while individual cell data are shown by the dots and squares.

J) Quantification of nuclear Nup62 intensity shows lower levels in C9-ALS iPSC neurons. Average signal is shown by graph bars while dots and squares represent the signal in individual neurons. The control group consists of two separate iPSC lines and C9orf72 is the combination of three C9-ALS iPSC lines.

Statistical significance in Fig 2C was determined by one-way ANOVA with Tukey post hoc analysis (Fig 2C) or two-tailed, unpaired students t-test (Fig 2E, F, G, I, J). * $p \leq 0.05$; ** $p \leq 0.01$; *** $p \leq 0.001$; **** $p \leq 0.0001$ vs control. Scale bar: 20 μm (A & B), 10 μm (D & G)

Figure 3

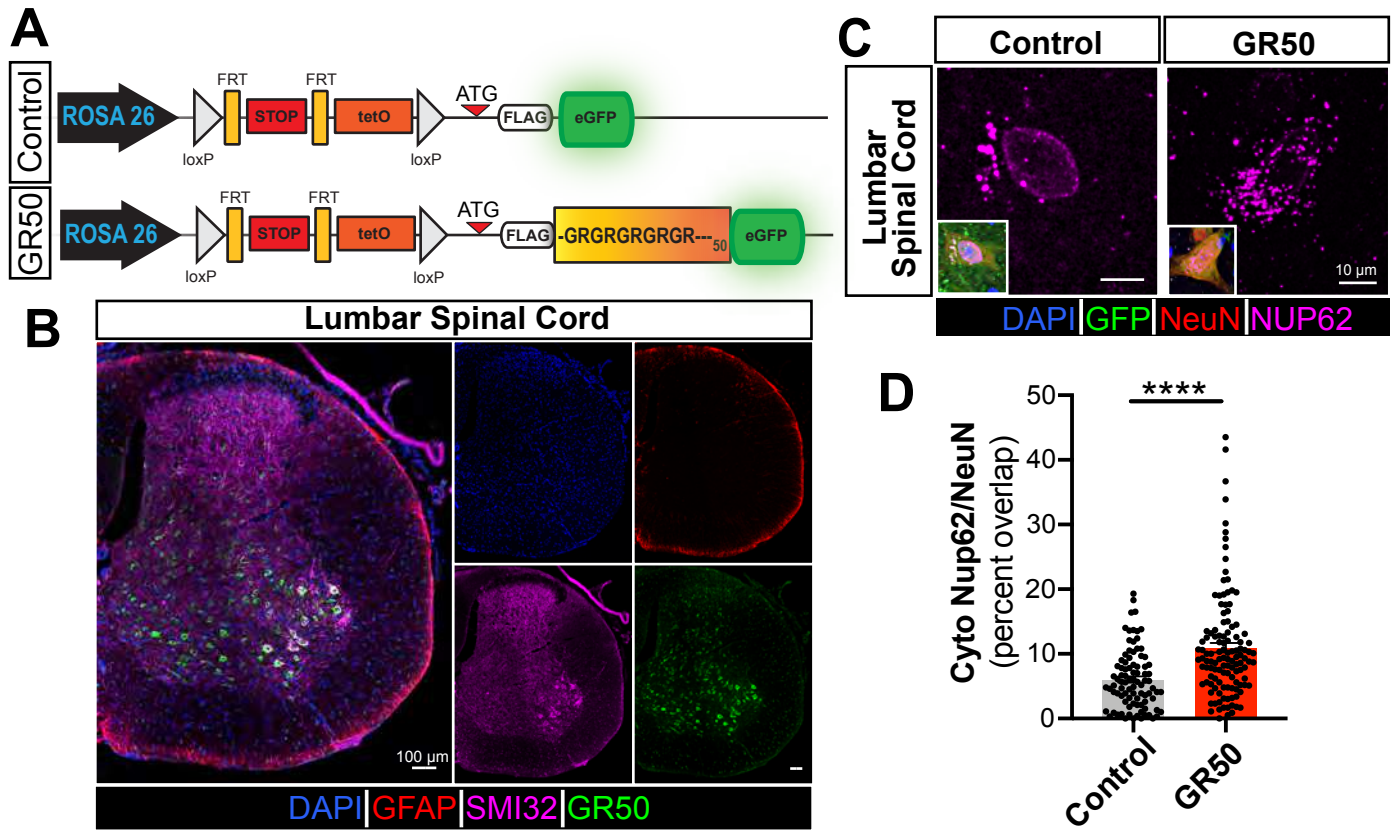


Figure 3. Nup62 is mislocalized in GR50-expressing spinal motor neurons *in vivo*

A) Top: Schematic of Flexible Accelerated Stop Tetracycline Operator (F.A.S.T.) Cassette driven by the ROSA26 promoter at the ROSA26 locus used to express ATG-driven FLAG-GR50-GFP (GR50) in C57BL/6 mice. The GR50 codon sequence is randomized to produce the dipeptide repeat protein in the absence of repeat-rich RNA. GR50 expression occurs upon crossing with a CAG-Cre mouse to excise the floxed STOP codon upstream of GR50. Bottom: The same cassette lacking the randomized GR50 sequence but still utilizing eGFP is used as the control.

B) Representative images of GR50 (green) expression in the lumbar spinal cord of a three-month-old homozygous male mouse. GFAP (red) and SMI32 (magenta) denote astrocytes from neurons, respectively.

C) Representative images of Nup62 (magenta) in GR50 (green) positive vs control in adult male mice.

D) Quantification of Nup62 cytosolic puncta area within NeuN-positive neurons of lumbar spinal cord are calculated as percent of Nup62 fluorescent signal area per ROI area.

Dots represent ROIs as measured by total NeuN expression per cell. N=3 mice, 90-122 ROIs per condition. **** $p \leq 0.0001$. Statistically significant differences were determined by Mann-Whitney test.

Figure 4

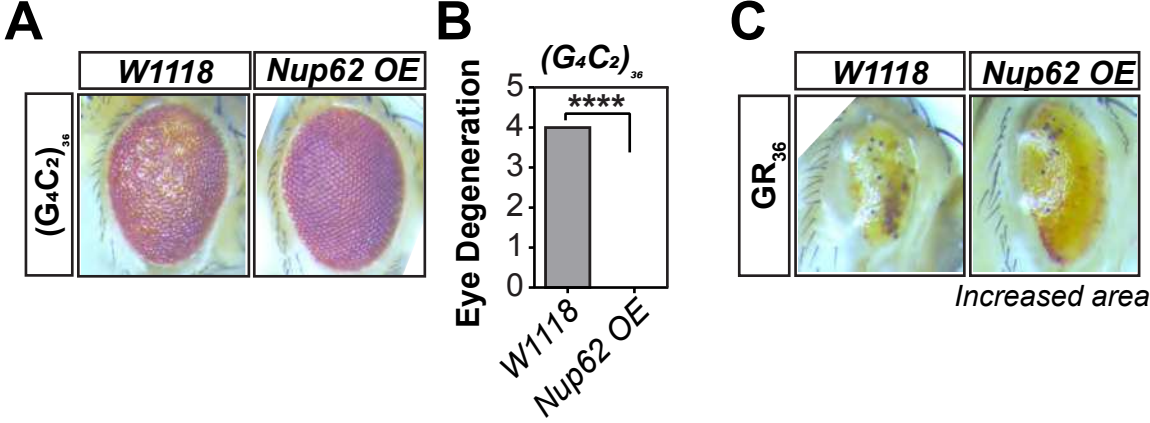


Figure 4. Nup62 restoration prevents neurotoxicity in C9-ALS/FTLD *Drosophila* models

A) Combination GMR-Gal4/TM3; Nup62 OE/Sb were crossed with UAS-(G4C2)₃₆ flies. Representative images are of flies carrying Nup62 overexpression or internal controls from the same cross carrying the Sb phenotype instead of Nup62 overexpression. Resulting progeny were evaluated within 24h of eclosion. W1118 phenotype *Drosophila* were used as control.

B) Degeneration of fly eye was scored according to previously described methods⁹⁵. We find Nup62 overexpression abolishes the (G4C2)₃₆ repeat expansion fly eye degeneration (n=3-4 flies per group).

C) Combination GMR-Gal4/TM3; Nup62 OE/Sb were crossed with UAS-(GR)₃₆ flies. Progeny were collected within 24h of eclosion and evaluated for fly eye degeneration. In the absence of Nup62 overexpression, the (GR)₃₆ progeny eyes show largely reduced eye size and an absence of ommatidial organization. However, Nup62 overexpression attenuates this effect (n=8-11 flies per group). W1118 phenotype *Drosophila* were used as control.

Statistical significance was determined by unpaired, two-tailed t-test when comparing two variables. **** $p \leq 0.0001$ vs control (W1118)

Figure 5

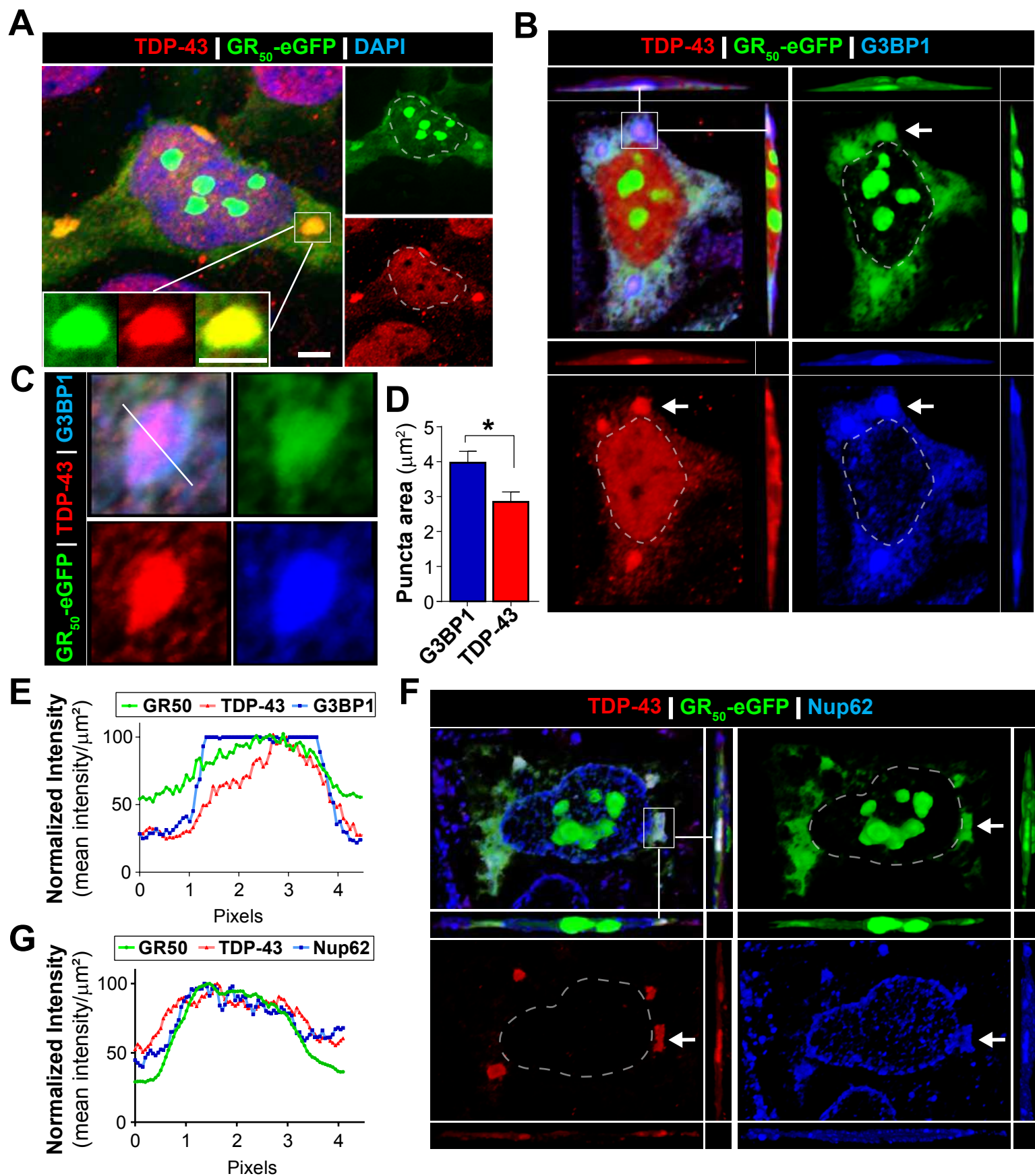


Figure 5. Poly-GR triggers SGs that recruit TDP-43 and Nup62

HEK293 cells were transfected with GR50-eGFP plasmid DNA and immunostained prior to imaging by confocal microscopy. Images reveal the accumulation of cytoplasmic GR50-eGFP condensates that we went on to characterize.

A) Maximum intensity projection image reveals endogenous TDP-43 and GR50-eGFP localize together in cytoplasmic condensates. Inset image highlights a single condensate containing GR50-eGFP and endogenous TDP-43.

B) Orthogonal view of cytoplasmic GR50-eGFP condensates in HEK293 cells reveals endogenous TDP-43 and SG marker G3BP1 exist within same three-dimensional space. Top left panel is a merged image and others are of individual channels.

C) Cropped image of cytoplasmic GR50-eGFP accumulations that we observe in cells. Immunocytochemistry for endogenous TDP-43 and G3BP1 reveal these proteins are detectable in the GR50-eGFP condensates.

D) G3BP1 (n=27) and TDP-43 (n=20) surface area was measured in GR50-eGFP⁺ condensates. We observe that TDP-43 is significantly smaller than G3BP1 in these GR50-eGFP structures.

E) Intensity profile plots for condensates containing GR50-eGFP, TDP-43, and G3BP1. An intensity profile plot line was drawn through the condensate and signal intensity is plotted across the length of line. This data further supports the hypothesis that these proteins exist within the same space.

F) Orthogonal view of cytoplasmic GR50-eGFP condensates in HEK293 cells reveals endogenous TDP-43 and Nup62 exist within same three-dimensional space. Top left panel is a merged image of all signals together and the other panels are of individual channels.

G) Intensity profile plots for condensate containing GR50-eGFP, TDP-43 and Nup62. An intensity profile plot line was drawn through the condensate and signal intensity is plotted across the length of line. This data further supports the hypothesis that these proteins exist within the same space.

Statistically significant differences were calculated by unpaired, two-tailed t-test. * $p \leq 0.05$ Scale bar: 5 μm

Figure 6. Cytoplasmic Nup62 and TDP-43 colocalization promotes insolubility

A) HEK293 cells were co-transfected with mRuby-Nup62 and eGFP-TDP43 (wild type). The cells were observed through live-scan confocal microscopy starting 3 hours after transfection and images were obtained every 5 min over the course of 15 h. Two populations of cytoplasmic mRuby-Nup62 condensates were observed: Reversible or irreversible. Reversible structures exhibit more dynamic activity and appear circular (see arrow). Irreversible structures appear less mobile or more static and have an angular structure (see asterisks). Schematic depicting characteristics of cytoplasmic mRuby-Nup62 structures is shown at bottom. Representative still images were obtained from the 6-10 h time points of the imaging session.

B) Quantification of Nup62 area in confocal microscopy images obtained during live imaging (5-15 h timepoints) described in Figure 6A. Irreversible condensates were significantly larger than reversible structures. The size of reversible granules was determined at times point immediately prior to dissipation. Irreversible granule area was calculated at final time point collected during live imaging session.

C) The percentage of reversible and irreversible mRuby-Nup62 granules containing eGFP-TDP43 were calculated throughout the duration of living imaging session (5-15 h timepoints) described in Figure 6A. A greater percentage of irreversible mRuby-Nup62 condensates contained eGFP-TDP43.

D) mRuby-Nup62 condensates were characterized for circularity score at the final time point of live image session (5-15 h timepoints) described in Figure 6A. Irreversible mRuby-Nup62 + eGFP-TDP43⁺ condensates had a significantly reduced circularity score relative to eGFP-TDP43⁻ and reversible mRuby-Nup62 + eGFP-TDP43⁺ condensates.

E) Representative FRAP analysis images of nuclear eGFP-TDP43 (reference solubility control) and cytoplasmic eGFP-TDP43 and mRuby-Nup62 condensates.

F) Quantification of FRAP analysis shows reduced fluorescence signal recovery in cytoplasmic eGFP-TDP43 and mRuby-Nup62 condensates relative to nuclear eGFP-TDP43 control.

G) HEK293 cells were co-transfected with mRuby-Nup62 and eGFP-TDP43 with NLS mutation point mutations (Δ NLS)¹³⁷. Cytoplasmic mRuby-Nup62 condensates do not colocalize with eGFP-TDP43 (Δ NLS).

Statistically significant differences were calculated by unpaired, two-tailed t-test or by one-way ANOVA with Tukey post hoc analysis. * $p \leq 0.05$; ** $p \leq 0.01$; **** $p \leq 0.0001$ vs control. Scale bar: 10 μ m

Figure 7

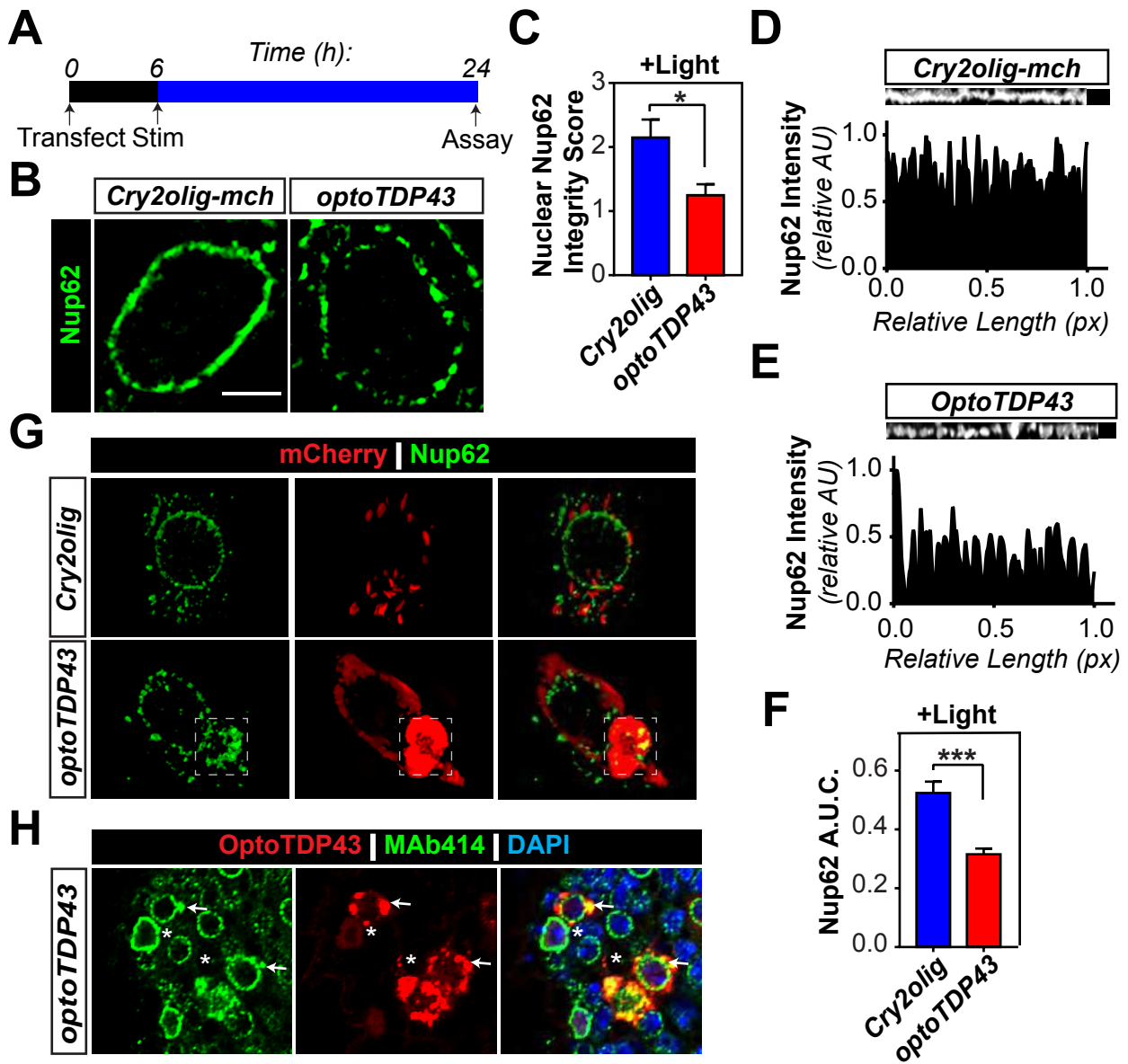


Figure 7. OptoTDP43 inclusions mislocalize Nup62

A) Schematic describing blue-light stimulation paradigm. HEK293 cells were transfected with OptoTDP43 or Cry2-Olig control constructs prior to 18h of blue light exposure.

B) Representative single slice (0.125 μm) N-SIM Super-resolution microscopy images of immunofluorescently-labelled Nup62 (green) in HEK293 cells. OptoTDP43⁺ cells exhibited the appearance of more fragmented Nup62 staining around nucleus.

C) Nuclear Nup62 integrity in N-SIM Super-resolution images was scored by blinded, unbiased observer. Scores are described in Supplemental Table 4. OptoTDP43⁺ cells received lower nuclear Nup62 integrity scores relative to control.

D-E) Representative raw data from control (Cry2-olig) and OptoTDP43 expressing cells shown in Fig 5D. Corresponding images of nuclear Nup62 staining are shown above graph.

F) Nuclear Nup62 fragmentation quantified according to intensity profile plots. Area under the curve (AUC) for Nup62 signal was averaged and expressed as a function of nuclear Nup62 circumference to account for variability in nuclear size.

G) N-SIM Super-resolution images of Control (Cry2-olig; top row) and OptoTDP43⁺ cells immunostained for Nup62 (green). Images revealed Nup62 sequestration into OptoTDP43 aggregates and this is highlighted by white box. Red signal depicts mCherry tag that is present on Cry2-Oligo and OptoTDP43 constructs.

H) Representative image of FG nups being sequestered into optoTDP43 aggregates in Optofly model. FG nups, such as Nup62, were detected by MAb414 antibody in the ventral nerve cord of third instar larvae after 24h of blue-light stimulation. Arrows highlight optoTDP43 aggregates that co-stain for MAb414 while asterisks indicated optoTDP43 aggregates that are FG nup negative.

In vitro sample size: n=7-10 cells/group. Statistical significance was determined by unpaired, two-tailed t-test. * $p \leq 0.05$, *** $p \leq 0.001$ vs control. Scale bar: 2.5 μm (B), 10 μm (H)

Figure 8

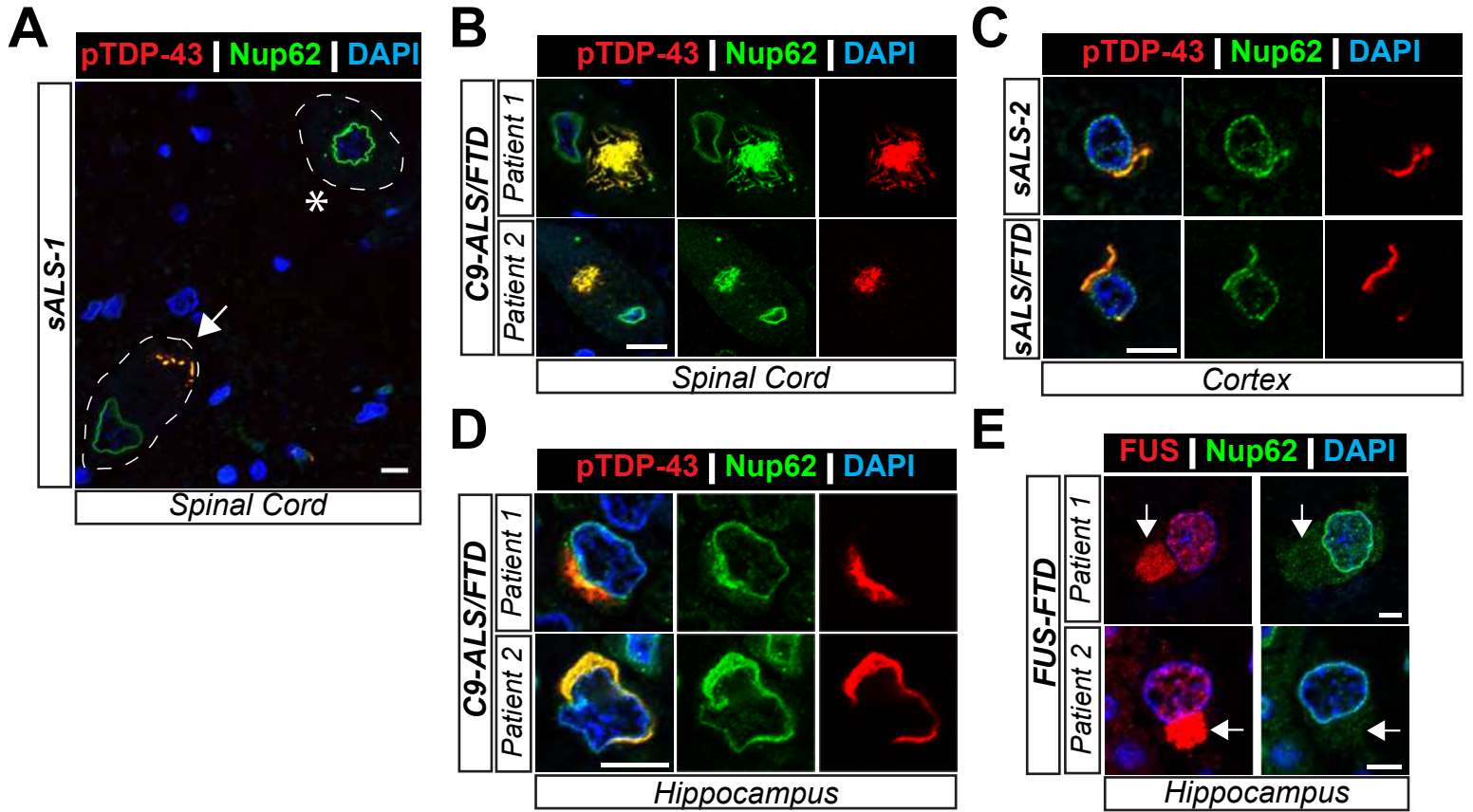


Figure 8. Nup62 colocalizes with pTDP-43 in C9-ALS/FTLD and sALS/FTLD

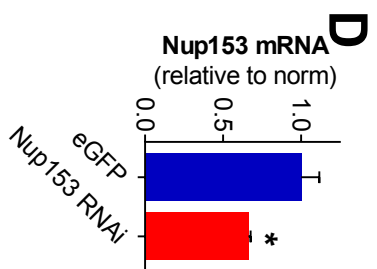
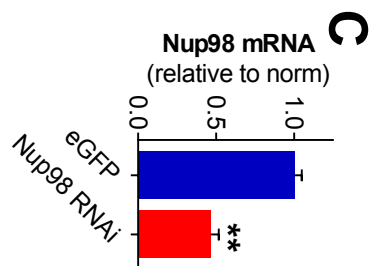
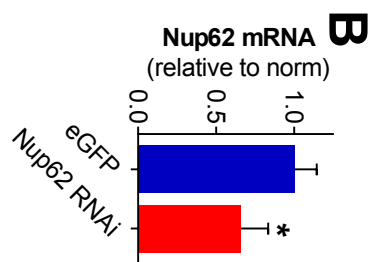
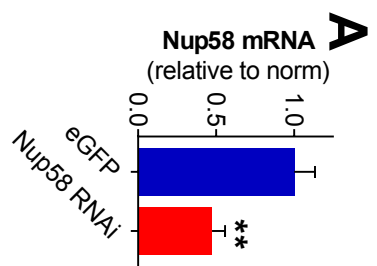
Nup62 (green) and phosphoTDP-43 (red) immunoreactivity in postmortem tissue from various clinical diagnoses (noted above images and Supplemental Table 3).

A-D) Intact nuclear Nup62 signal surrounds DAPI⁺ nuclei (asterisks) but becomes more diffuse in cells exhibiting cytoplasmic phosphoTDP-43 (arrowhead). Colocalization of Nup62 and phosphoTDP-43 accumulations were observed in the spinal cord (A & B), cortex (C), and hippocampus (D). Patient diagnostic classifications are described in Supplemental Table 3.

E) Cytoplasmic FUS accumulations (red, arrows) in the hippocampus from two FTLN patients do not show Nup62 localization.

Scale bar: 10 μ m

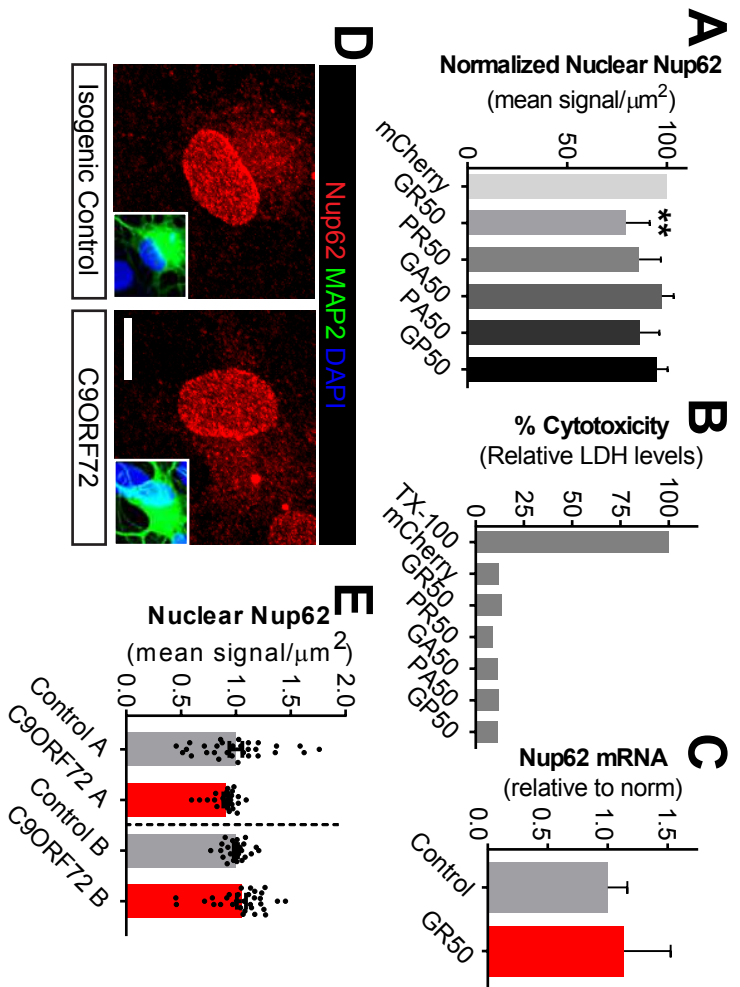
Supplemental Figure 1



Supplemental Figure 1. Validation of FG Nup knockdown in Drosophila RNAi models.

mRNA was extracted from Drosophila fly heads and qPCR analysis confirmed downregulation of FG Nup mRNA levels. A minimum of 9 fly heads were pulled together for each group and run-in triplicate technical replicates. Normalization of gene levels were expressed relative to alpha-tubulin. Statistically significant differences between control and RNAi fly lines were determined by unpaired student's t-test * $p \leq 0.05$; ** $p \leq 0.01$ vs eGFP control.

Supplemental Figure 2



Supplemental Figure 2. Poly-GR causes nuclear Nup62 deficits at subtoxic concentrations.

A) Quantification of nuclear Nup62 levels by immunofluorescence staining reveals that deficits are associated with poly-GR expression relative to control (mCherry-expressing). Representative image is shown in Fig 2.

B) Cell death was measured by LDH cytotoxicity assay in HEK293 cells expressing the dipeptide repeat protein construct for 24h. TX-100-treated HEK293 cells were included during assay as a positive measure of cell death. No significant increase in cell death was observed in cells expressing dipeptide repeat proteins relative to Control group.

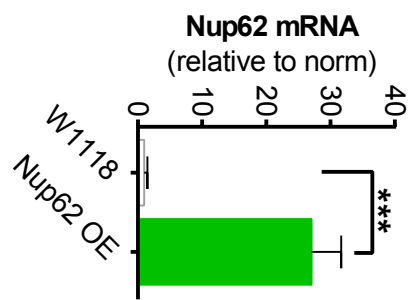
C) Nup62 transcript levels were measured in HEK293 cells after 24h of transfection with GR50-eGFP plasmid DNA and showed no significant difference between groups. Normalization of gene levels were expressed relative to GAPDH.

D) iPSCs were differentiated and matured for 28 days into motor-neuron enriched cultures. Cells were stained for Nup62 and MAP2 in order to determine whether nuclear Nup62 defects occurred at this stage of culturing. Representative maximum intensity image is shown.

E) Two separate C9-ALS iPSC lines (A & B) and their isogenic control (A & B, respectively) images were acquired by confocal microscopy and revealed no significant difference in nuclear Nup62 mean intensity from maximum intensity projection images. (n=30-32 cells/group)

Statistical significance was determined by one-way ANOVA with Tukey post-hoc analysis. ** $p \leq 0.01$ vs control. Scale bar: 10 μ m

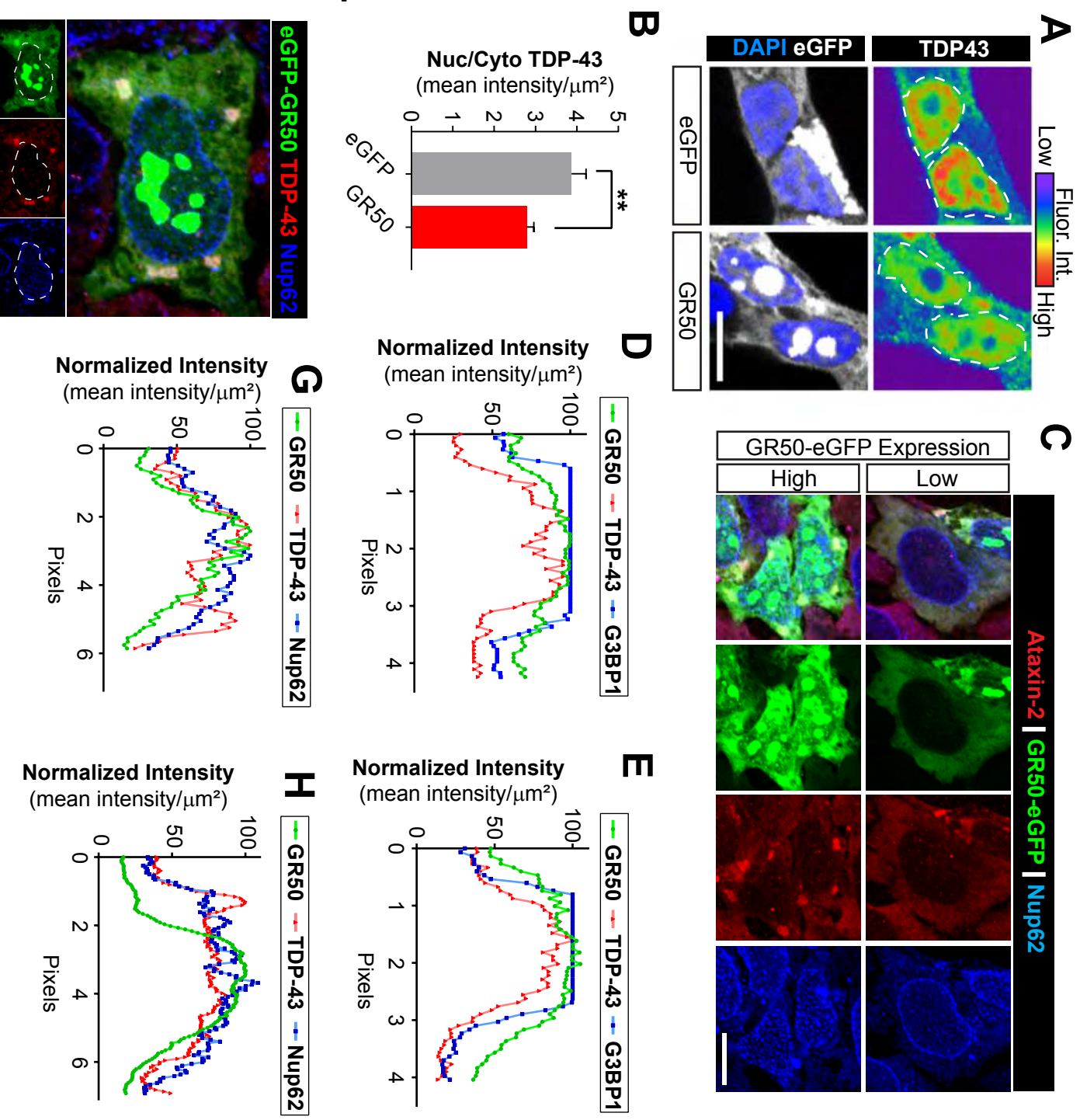
Supplemental Figure 3



Supplemental Figure 3. Validation of Nup62 overexpression Drosophila model

mRNA was extracted from Drosophila fly heads and qPCR analysis confirmed increased Nup62 transcript levels in the Nup62 overexpression fly (Nup62 OE). A minimum of 9 fly heads were pulled together for each group and run-in triplicate technical replicates. Normalization of gene levels were expressed relative to alpha-tubulin. Statistically significant differences between control and Nup62 overexpression fly lines were determined by unpaired student's t-test *** $p \leq 0.001$ vs W1118 control.

Supplemental Figure 4



Supplemental Figure 4. Aberrant TDP-43 alters FG Nup62

A) Image depicting TDP-43 distribution in HEK293 cells expressing GR50-eGFP or eGFP control plasmid DNA. TDP-43 immunostaining is presented in spectral colors. Warmer colors represent higher TDP-43 levels while cooler colors show lower TDP-43 levels. DAPI is presented in blue and eGFP or GR50-eGFP constructs are shown in white.

B) Quantification of nuclear and cytoplasmic distribution of TDP-43 signal in confocal images. Regions of interest (ROIs) were drawn around DAPI or cytoplasmic signal to determine TDP-43 in their respective regions (n=27-53 cells/group). Nuclear area was determined according to DAPI⁺ staining and cytoplasmic region was determined by non-nuclear eGFP signal.

C) HEK293 cells were transfected with 200 ng GR50-eGFP plasmid DNA for 24h and immunostained for SG marker Ataxin-2 and Nup62. Cells expressing low (top row) and high (bottom row) levels of GR50-eGFP are represented. We observe the formation of Ataxin-2⁺ accumulations with high GR50-eGFP expression levels. Nup62 is detected in cytoplasmic Ataxin-2⁺ condensates.

D-E) Intensity profile plots of additional cytoplasmic GR50-eGFP condensates. An intensity profile plot line was drawn through the condensate and signal intensity is plotted across the length of line. This data further supports the hypothesis that GR50-eGFP, G3BP1, and TDP-43 exist within the same space.

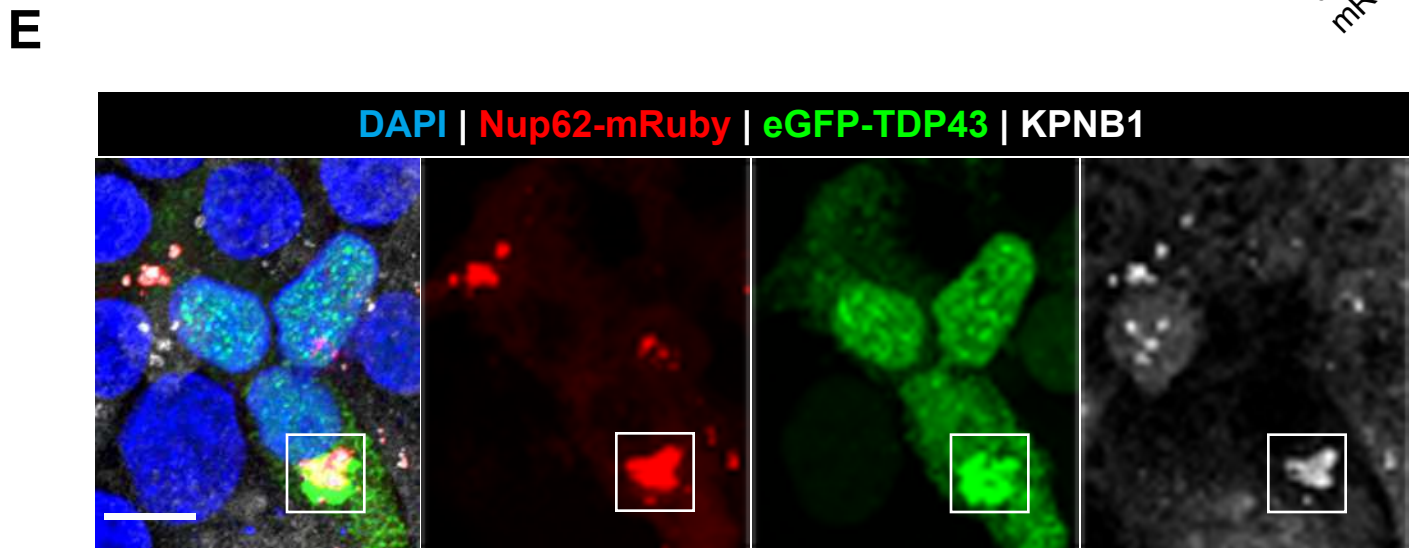
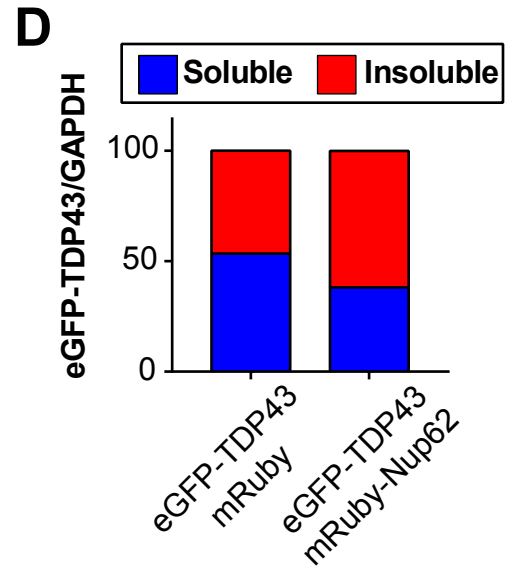
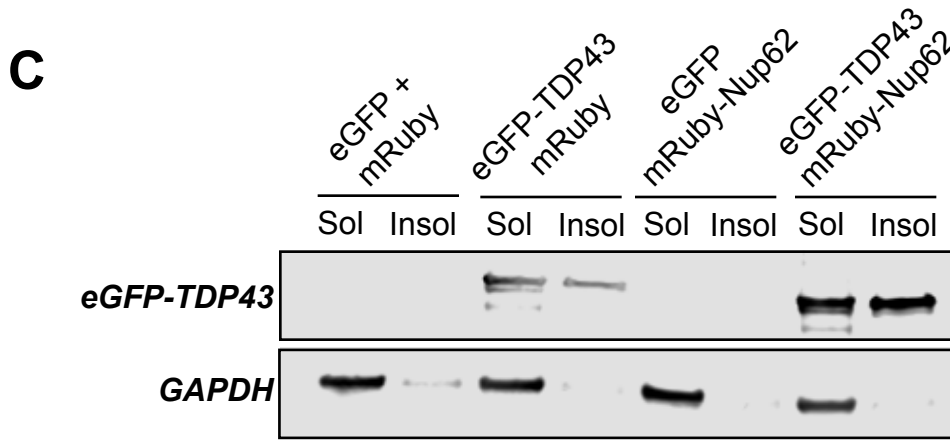
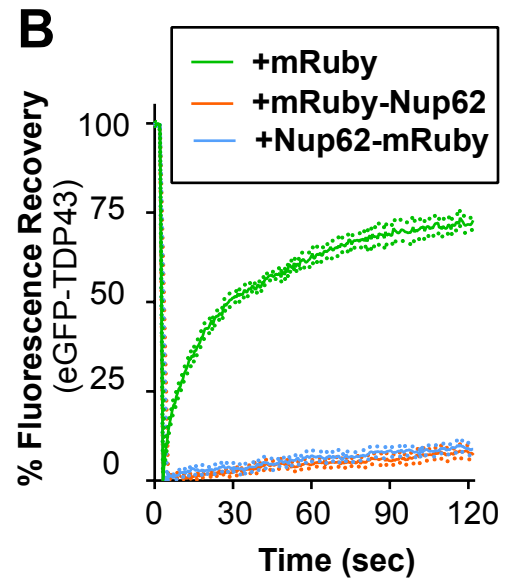
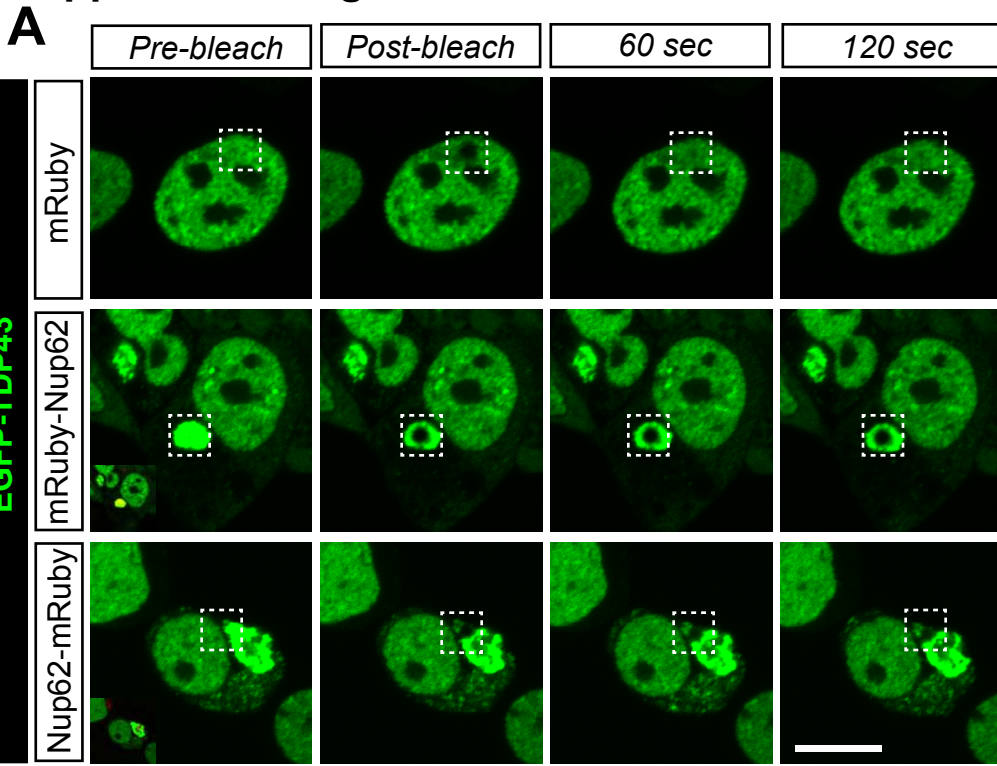
F) GR50-eGFP transfected HEK293 cells were also immunostained for TDP-43 and Nup62. Maximum intensity projection confocal image reveals colocalization of TDP-43 and Nup62 in cytoplasmic GR50-eGFP condensates. Top image is a merge of all channels and individual signals are presented below.

G-H) Intensity profile plots of additional cytoplasmic GR50-eGFP condensates with TDP-43 and Nup62. An intensity profile plot line was drawn through the condensate and signal intensity is

plotted across the length of line. This data further supports the hypothesis that GR50-eGFP, TDP-43 and Nup62 exist within the same space.

Statistically significant difference between control and GR50 expression groups was determined by two-tailed, unpaired t-test. ** $p \leq 0.01$ vs control. Scale bar: 10 μm

Supplemental Figure 5



Supplemental Figure 5. Cytoplasmic mRuby-Nup62 condensates disrupt eGFP-TDP43 solubility

A) HEK293 cells were co-transfected with EGFP-TDP43 and mRuby, mRuby-Nup62, or Nup62-mRuby to determine whether both orientations of Nup62 form insoluble, cytoplasmic TDP43 structures. Representative FRAP analysis images of eGFP-TDP43 are shown. White box indicates region of FRAP.

B) Quantification of FRAP analysis shows both mRuby-Nup62 and Nup62-mRuby reduce eGFP-TDP43 fluorescent signal recovery.

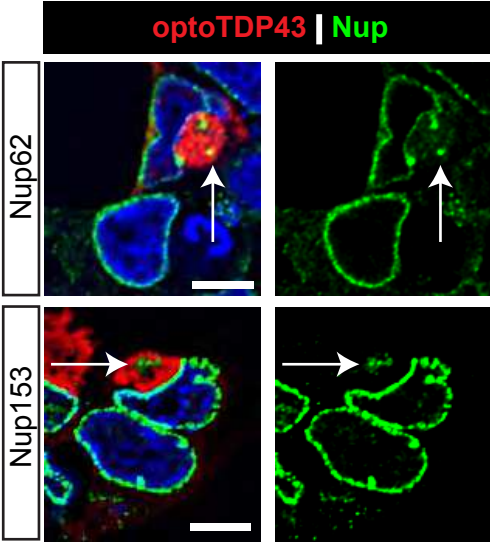
C) Representative western blot image of shift in eGFP-TDP43 into insoluble fraction.

D) Quantification of soluble and insoluble eGFP-TDP43 by western blot analysis.

E) HEK293 cells co-transfected with Nup62-mRuby and eGFP-TDP43. Cytoplasmic Nup62-mRuby structures show KPNB1 co-localization by immunofluorescent staining.

Scale bar: 10 μ m

Supplemental Figure 6



Supplemental Figure 6. FG nups localize to OptoTDP43 aggregates

The effect of OptoTDP43 on two FG Nups, Nup153 and Nup62, was assessed in HEK293 cells. Nup62 and another FG Nup, Nup153, were assessed in HEK293 cells with OptoTDP43 aggregates following blue-light stimulation. Nup62 and Nup153 were detected by immunofluorescent staining and confocal microscopy. Images presented are maximum intensity projections. Nup62 and Nup153 (green) in OptoTDP43 aggregates (red) are indicated by arrow.

Figures

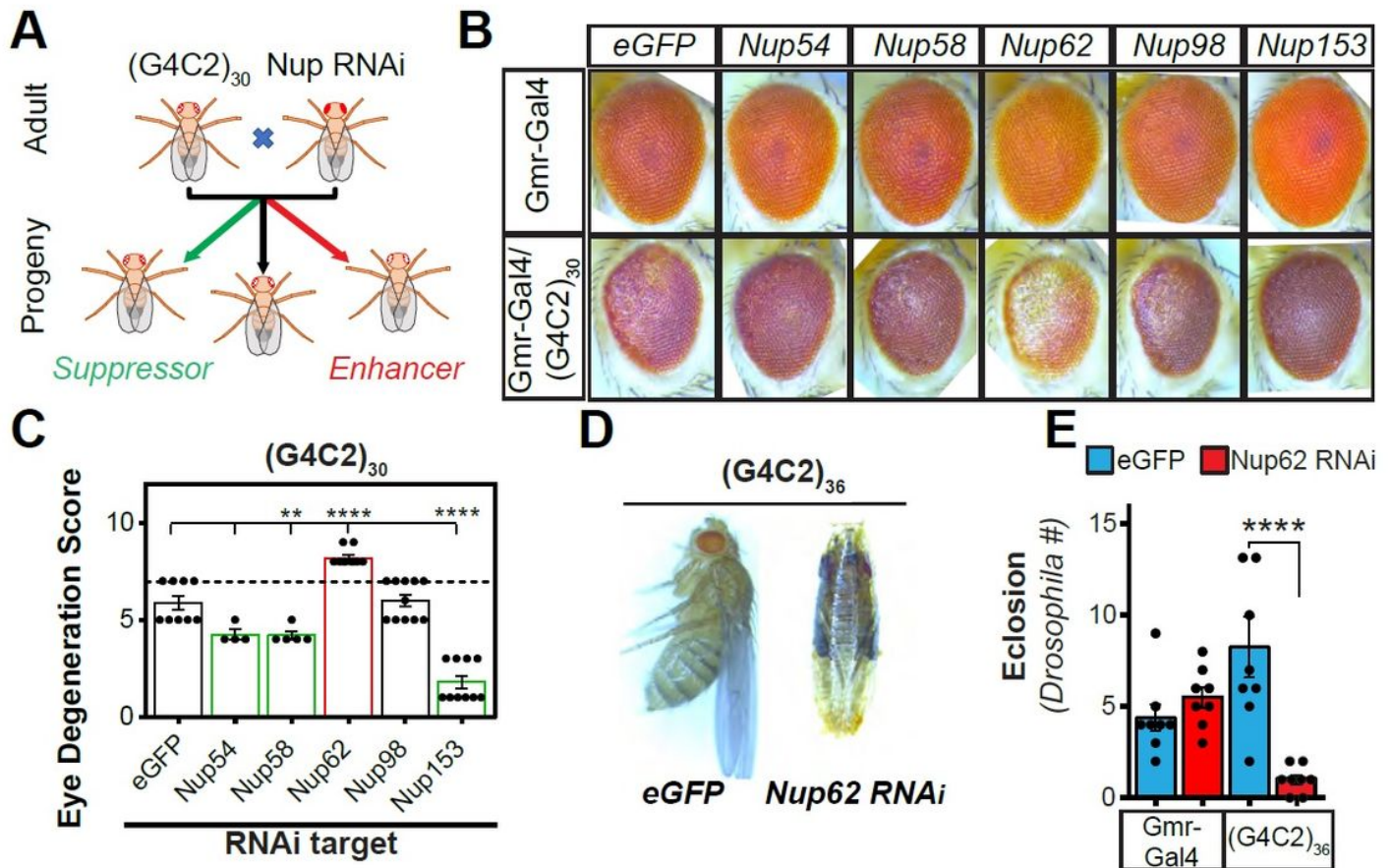


Figure 1

FG Nucleoporins are genetic modifiers of the G4C2 repeat expansion in *Drosophila*. A) Schematic describing the methods used to identify genetic modifiers of G4C2 repeat expansion-mediated degeneration. A reduction in G4C2 repeat expansion fly eye degeneration Nup RNAi is classified as a genetic suppressor while increases are identified as genetic enhancers. B) Representative images of fly eyes from GMR-Gal4 wild-type (top row) or (G4C2)₃₀ repeat expansion (bottom row) flies combined with control or UAS-Nup RNAi flies. C) Quantification of scored fly eye degeneration. Unchanged degeneration score is shown by black bars while genetic modifiers that increase eye degeneration are in red (enhancer) or reduce eye degeneration are in green (suppressor) eye degeneration relative to (G4C2)₃₀ repeat expansion + eGFP control. The dashed horizontal line indicates the score for (G4C2)₃₀ repeat expansion eye degeneration alone. D) Combination GMR-Gal4; (G4C2)₃₆ repeat expansion were crossed with a UAS-Nup62 RNAi or UAS-eGFP fly. Shown are representative images of these flies 0-1 day post eclosion. E) Bar graph shows the quantification for (G4C2)₃₆ repeat expansion fly eclosion in the presence and absence of Nup62 RNAi. The bars show average eclosion over the course of eight days while individual dots are representative of fly counts for one 24 h eclosion period. (G4C2)₃₆;GMR-GAL4 line crossed with UAS-EGFP fly line was used as the control group. Statistically significant differences in fly eye degeneration was determined by one-way ANOVA with Tukey's

multiple comparison's test: ** $p \leq 0.01$; **** $p \leq 0.0001$ vs control. Statistically significant differences in eclosion frequency was determined by one-way ANOVA with Dunnett's multiple comparison's test: **** $p \leq 0.0001$ vs UAS-EGFP x (G4C2)₃₆ repeat expansion fly.

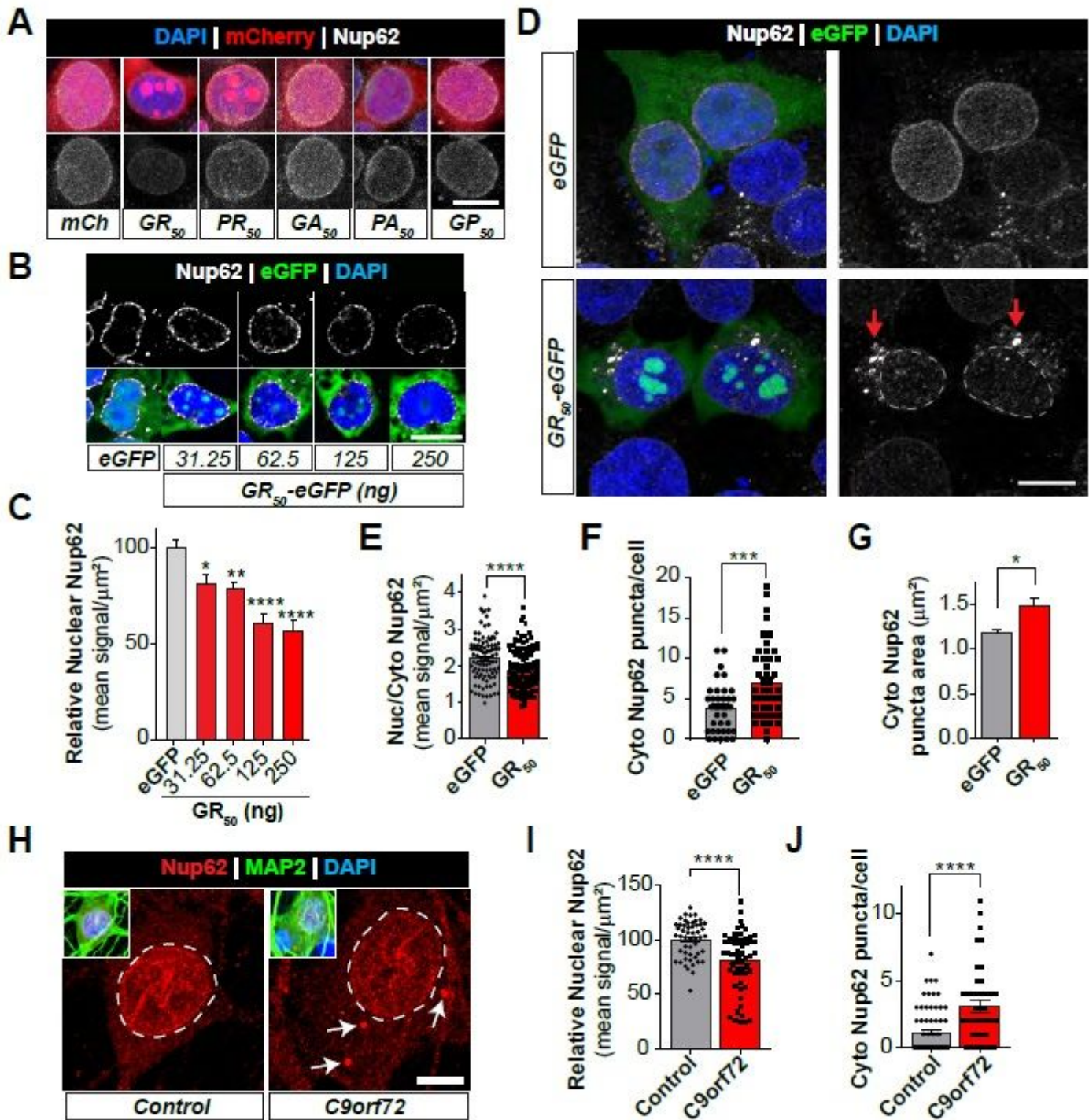


Figure 2

Poly-GR alters Nup62 localization in vitro. A) Nuclear Nup62 (white) levels were assessed in HEK293 cells expressing mCherry-tagged poly-DPR constructs (red) by immunofluorescent staining and confocal microscopy. Representative maximum intensity projection images are shown. Nuclear Nup62

quantification is shown in Supplemental Fig 2A. B) HEK293 cells were transfected with increasing amounts of GR50-eGFP plasmid DNA and immunostained for Nup62. Images were processed by automatic deconvolution in Nikon Elements. Single slice images (0.2 μm) of Nup62 (white) show dose-dependent reduction in nuclear Nup62 with increasing GR50-eGFP plasmid DNA. Scale bar: 20 μm C) Nuclear Nup62 signal was quantified in maximum intensity projection confocal images following immunofluorescent staining (n=47-93 cells/group). Data corresponds to images presented in Fig 2B. D) To assess whether GR50-eGFP alters nuclear Nup62 localization, HEK293 cells were transfected with eGFP (Control) or GR50-eGFP (green) and immunostained for Nup62 (white). Representative confocal images show nuclear Nup62 depletion that coincides with cytoplasmic Nup62 puncta accumulation. Nuclear compartment is highlighted by dashed white line and cytoplasmic Nup62 accumulations are indicated by red arrow. E) Quantification of nuclear/cytoplasmic distribution of Nup62 signal corresponding to Fig 2D representative images. Regions of interest (ROIs) were drawn around DAPI or cytoplasm signals to determine Nup62 in the respective regions. The distribution for each cell was determined and then averaged for n=96-138 cells across four independent experiments. F) We identified cytoplasmic Nup62 puncta by spot detection (diameter 1 μm or larger) methods and counted the frequency of these structures in each HEK293 cell (n=39-47 cells). Quantification reveals an increased cytoplasmic Nup62 prevalence due to GR50 expression. G) Cytoplasmic Nup62 puncta were detected by ROI automatic detection and quantification reveals GR50-eGFP causes a significant increase in their size relative to eGFP control. H) Nup62 immunostaining (red) is shown in the representative confocal maximum intensity projection images of healthy control and C9-ALS MAP2+ iPSC neurons that had been matured and differentiated for 89 days. DAPI+ nuclear compartment is highlighted with dashed white line and cytoplasmic Nup62 puncta are indicated by white arrows. I) The number of Nup62 puncta in MAP2+ iPSC neurons is quantified from confocal images represented in Figure 2G. Data analysis reveals an increase in cytoplasmic Nup62 puncta quantity in C9orf72 iPSC neurons. Average cytoplasmic Nup62 puncta per cell are shown by the graph bars while individual cell data are shown by the dots and squares. J) Quantification of nuclear Nup62 intensity shows lower levels in C9-ALS iPSC neurons. Average signal is shown by graph bars while dots and squares represent the signal in individual neurons. The control group consists of two separate iPSC lines and C9orf72 is the combination of three C9-ALS iPSC lines. Statistical significance in Fig 2C was determined by one-way ANOVA with Tukey post hoc analysis (Fig 2C) or two-tailed, unpaired students t-test (Fig 2E, F, G, I, J). * $p \leq 0.05$; ** $p \leq 0.01$; *** $p \leq 0.001$; **** $p \leq 0.0001$ vs control. Scale bar: 20 μm (A & B), 10 μm (D & G)

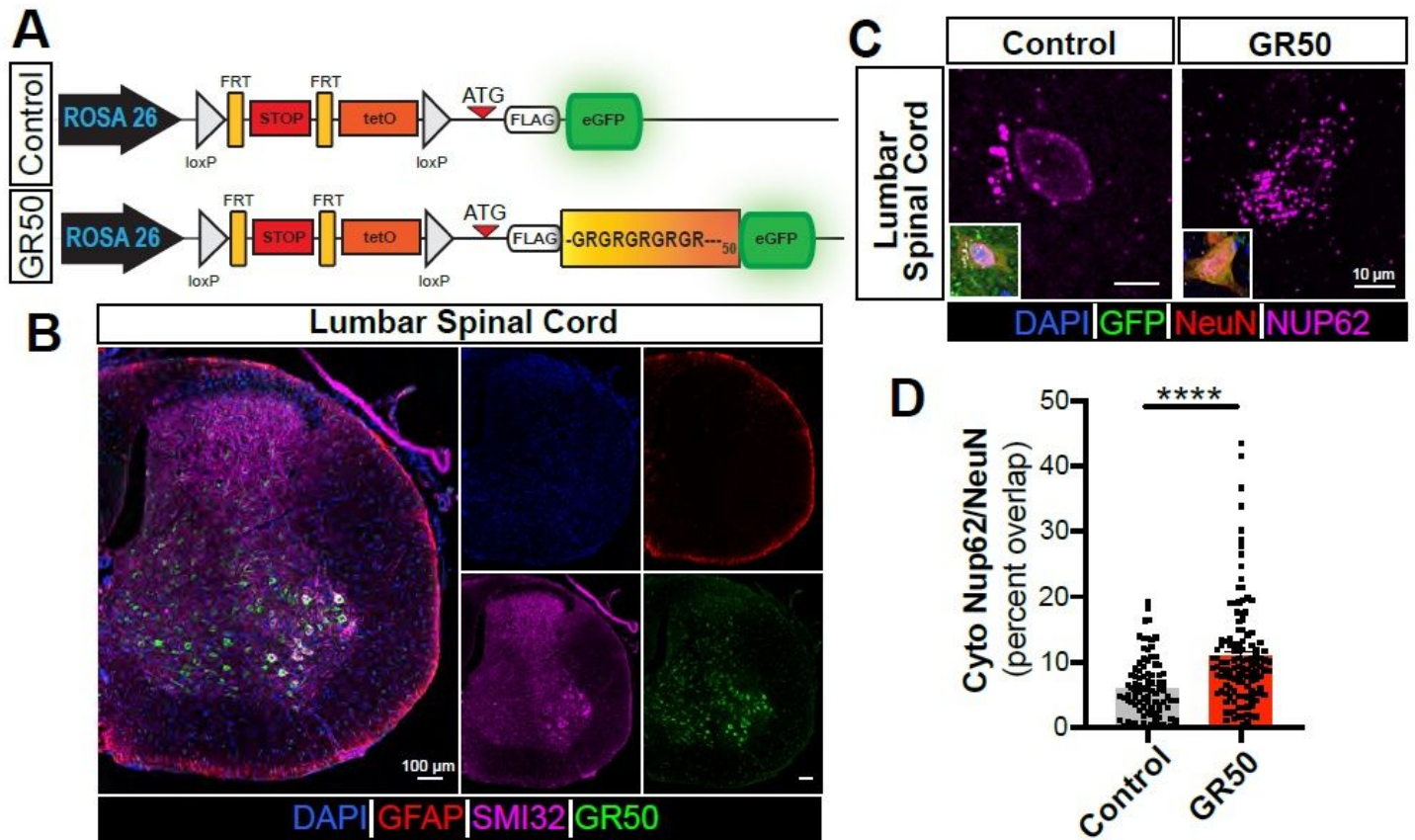


Figure 3

Nup62 is mislocalized in GR50-expressing spinal motor neurons in vivo A) Top: Schematic of Flexible Accelerated Stop Tetracycline Operator (F.A.S.T.) Cassette driven by the ROSA26 promoter at the ROSA26 locus used to express ATG-driven FLAG-GR50-GFP (GR50) in C57BL/6 mice. The GR50 codon sequence is randomized to produce the dipeptide repeat protein in the absence of repeat-rich RNA. GR50 expression occurs upon crossing with a CAG-Cre mouse to excise the floxed STOP codon upstream of GR50. Bottom: The same cassette lacking the randomized GR50 sequence but still utilizing eGFP is used as the control. B) Representative images of GR50 (green) expression in the lumbar spinal cord of a three-month-old homozygous male mouse. GFAP (red) and SMI32 (magenta) denote astrocytes from neurons, respectively. C) Representative images of Nup62 (magenta) in GR50 (green) positive vs control in adult male mice. D) Quantification of Nup62 cytosolic puncta area within NeuN-positive neurons of lumbar spinal cord are calculated as percent of Nup62 fluorescent signal area per ROI area. Dots represent ROIs as measured by total NeuN expression per cell. N=3 mice, 90-122 ROIs per condition. **** $p \leq 0.0001$. Statistically significant differences were determined by Mann-Whitney test.

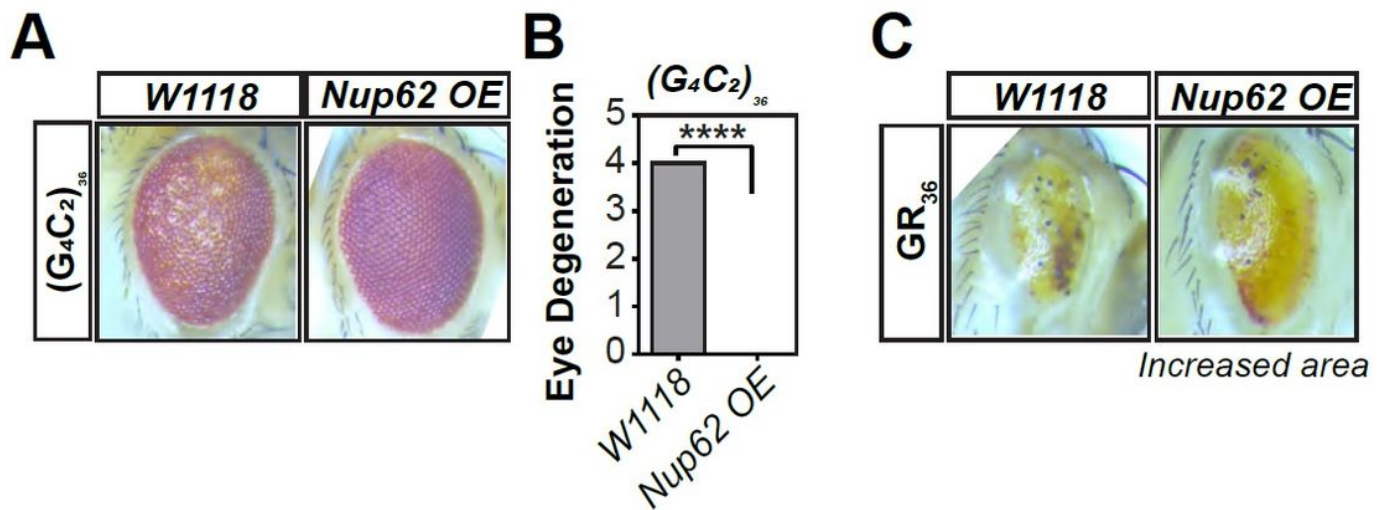


Figure 4

Nup62 restoration prevents neurotoxicity in C9-ALS/FTLD *Drosophila* models A) Combination GMR-Gal4/TM3; Nup62 OE/Sb were crossed with UAS-(G4C2)₃₆ flies. Representative images are of flies carrying Nup62 overexpression or internal controls from the same cross carrying the Sb phenotype instead of Nup62 overexpression. Resulting progeny were evaluated within 24h of eclosion. W1118 phenotype *Drosophila* were used as control. B) Degeneration of fly eye was scored according to previously described methods⁹⁵. We find Nup62 overexpression abolishes the (G4C2)₃₆ repeat expansion fly eye degeneration (n=3-4 flies per group). C) Combination GMR-Gal4/TM3; Nup62 OE/Sb were crossed with UAS-(GR)₃₆ flies. Progeny were collected within 24h of eclosion and evaluated for fly eye degeneration. In the absence of Nup62 overexpression, the (GR)₃₆ progeny eyes show largely reduced eye size and an absence of ommatidial organization. However, Nup62 overexpression attenuates this effect (n=8-11 flies per group). W1118 phenotype *Drosophila* were used as control. Statistical significance was determined by unpaired, two-tailed t-test when comparing two variables. **** p ≤ 0.0001 vs control (W1118)

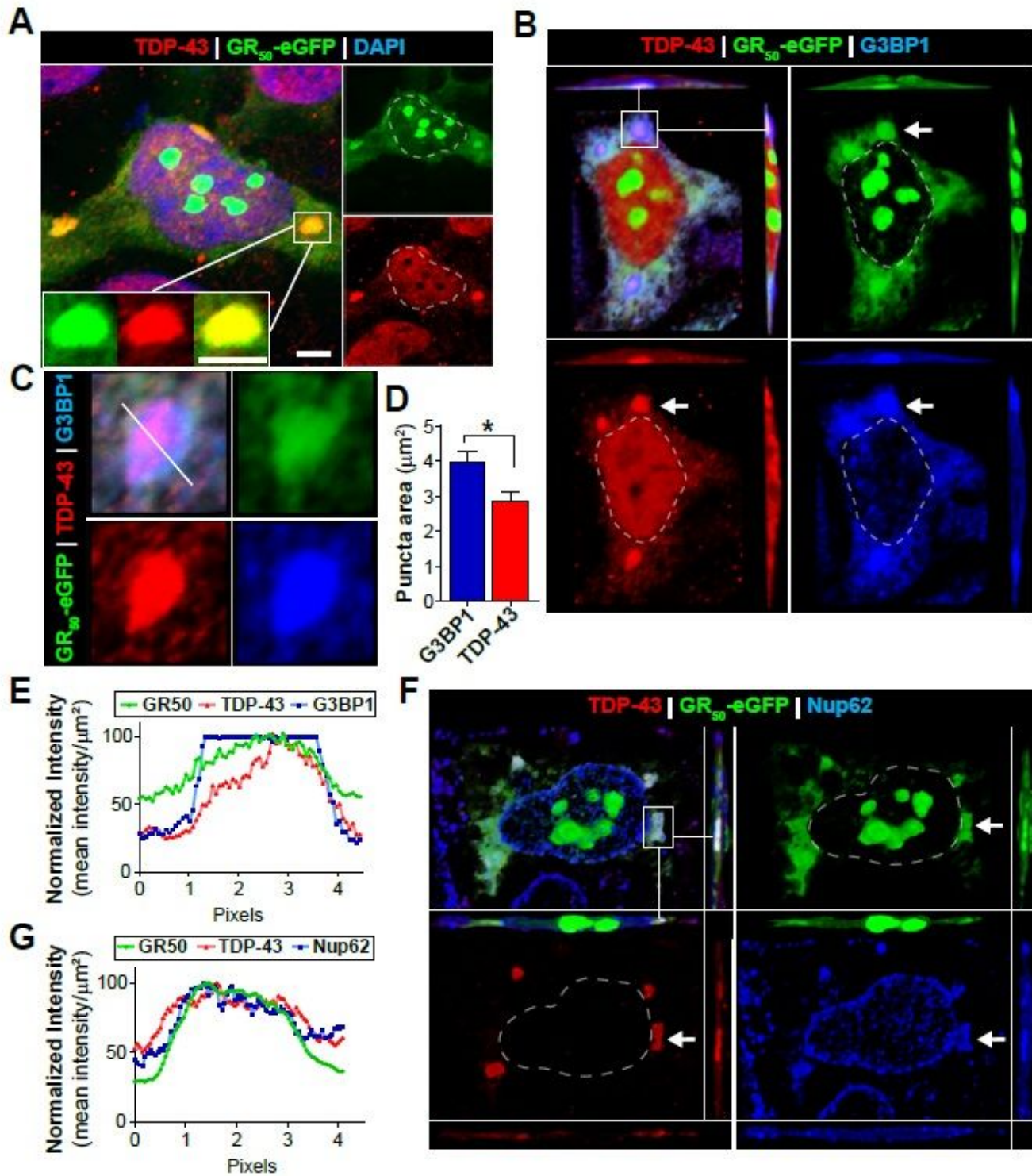


Figure 5

Poly-GR triggers SGs that recruit TDP-43 and Nup62 HEK293 cells were transfected with GR50-eGFP plasmid DNA and immunostained prior to imaging by confocal microscopy. Images reveal the accumulation of cytoplasmic GR50-eGFP condensates that we went on to characterize. A) Maximum intensity projection image reveals endogenous TDP-43 and GR50-eGFP localize together in cytoplasmic condensates. Inset image highlights a single condensate containing GR50-eGFP and endogenous TDP-

43. B) Orthogonal view of cytoplasmic GR50-eGFP condensates in HEK293 cells reveals endogenous TDP-43 and SG marker G3BP1 exist within same three-dimensional space. Top left panel is a merged image and others are of individual channels. C) Cropped image of cytoplasmic GR50-eGFP accumulations that we observe in cells. Immunocytochemistry for endogenous TDP-43 and G3BP1 reveal these proteins are detectable in the GR50-eGFP condensates. D) G3BP1 (n=27) and TDP-43 (n=20) surface area was measured in GR50-eGFP+ condensates. We observe that TDP-43 is significantly smaller than G3BP1 in these GR50-eGFP structures. E) Intensity profile plots for condensates containing GR50-eGFP, TDP-43, and G3BP1. An intensity profile plot line was drawn through the condensate and signal intensity is plotted across the length of line. This data further supports the hypothesis that these proteins exist within the same space. F) Orthogonal view of cytoplasmic GR50-eGFP condensates in HEK293 cells reveals endogenous TDP-43 and Nup62 exist within same three-dimensional space. Top left panel is a merged image of all signals together and the other panels are of individual channels. G) Intensity profile plots for condensate containing GR50-eGFP, TDP-43 and Nup62. An intensity profile plot line was drawn through the condensate and signal intensity is plotted across the length of line. This data further supports the hypothesis that these proteins exist within the same space. Statistically significant differences were calculated by unpaired, two-tailed t-test. * $p \leq 0.05$ Scale bar: 5 μm

Irreversible structures appear less mobile or more static and have an angular structure (see asterisks). Schematic depicting characteristics of cytoplasmic mRuby-Nup62 structures is shown at bottom. Representative still images were obtained from the 6-10 h time points of the imaging session. B) Quantification of Nup62 area in confocal microscopy images obtained during live imaging (5- 15 h timepoints) described in Figure 6A. Irreversible condensates were significantly larger than reversible structures. The size of reversible granules was determined at times point immediately prior to dissipation. Irreversible granule area was calculated at final time point collected during live imaging session. C) The percentage of reversible and irreversible mRuby-Nup62 granules containing eGFP-TDP43 were calculated throughout the duration of living imaging session (5-15 h timepoints) described in Figure 6A. A greater percentage of irreversible mRuby-Nup62 condensates contained eGFPTDP43. D) mRuby-Nup62 condensates were characterized for circularity score at the final time point of live image session (5-15 h timepoints) described in Figure 6A. Irreversible mRuby-Nup62 + eGFPTDP43+ condensates had a significantly reduced circularity score relative to eGFP-TDP43- and reversible mRuby-Nup62 + eGFP-TDP43+ condensates. E) Representative FRAP analysis images of nuclear eGFP-TDP43 (reference solubility control) and cytoplasmic eGFP-TDP43 and mRuby-Nup62 condensates. F) Quantification of FRAP analysis shows reduced fluorescence signal recovery in cytoplasmic eGFP-TDP43 and mRuby-Nup62 condensates relative to nuclear eGFP-TDP43 control. G) HEK293 cells were co-transfected with mRuby-Nup62 and eGFP-TDP43 with NLS mutation point mutations (Δ NLS)¹³⁷. Cytoplasmic mRuby-Nup62 condensates do not colocalize with eGFPTDP43 (Δ NLS). Statistically significant differences were calculated by unpaired, two-tailed t-test or by one-way ANOVA with Tukey post hoc analysis. * $p \leq 0.05$; ** $p \leq 0.01$; **** $p \leq 0.0001$ vs control. Scale bar: 10 μ m

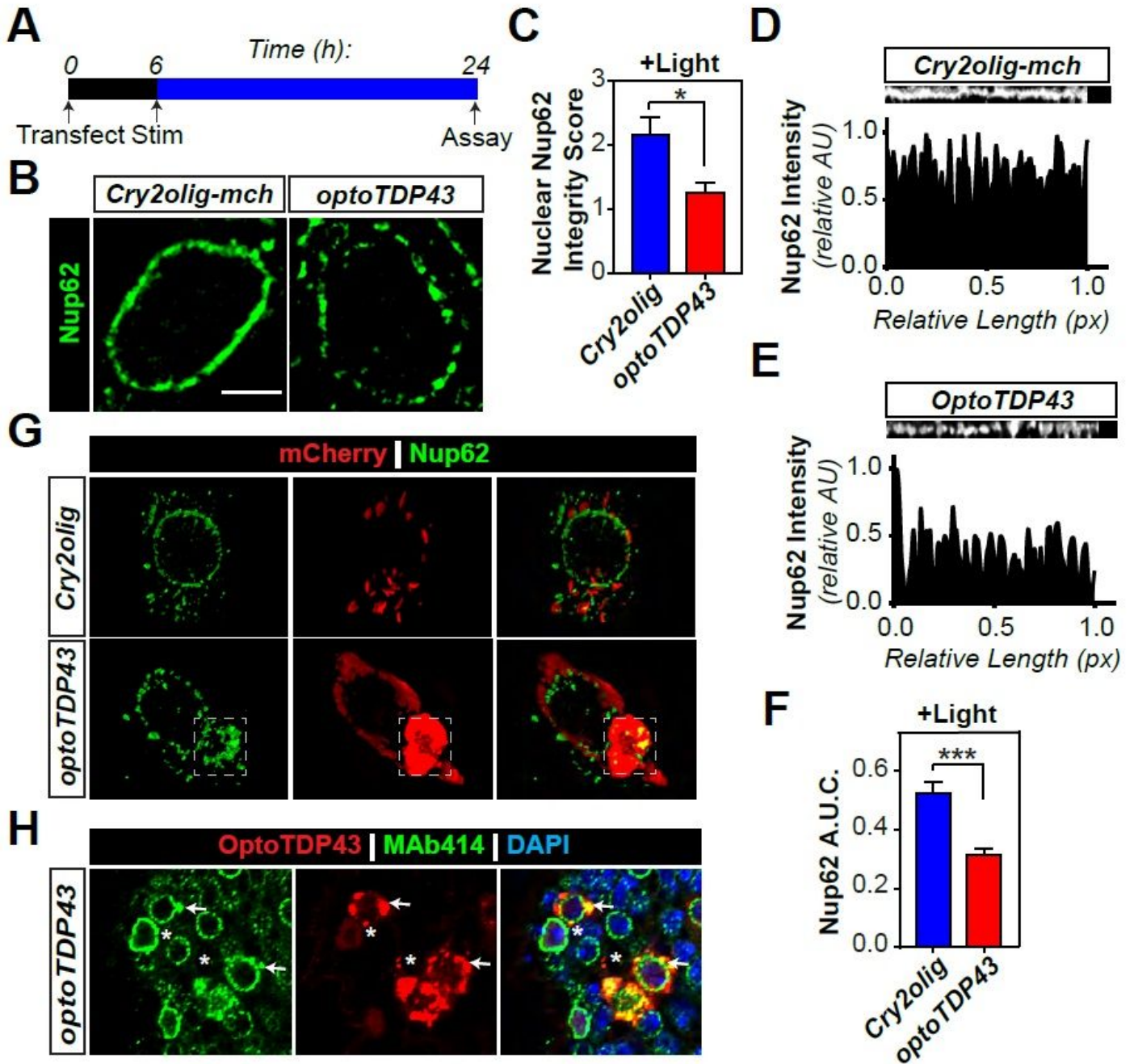


Figure 7

OptoTDP43 inclusions mislocalize Nup62 A) Schematic describing blue-light stimulation paradigm. HEK293 cells were transfected with OptoTDP43 or Cry2-Olig control constructs prior to 18h of blue light exposure. B) Representative single slice (0.125 μm) N-SIM Super-resolution microscopy images of immunofluorescently-labelled Nup62 (green) in HEK293 cells. OptoTDP43+ cells exhibited the appearance of more fragmented Nup62 staining around nucleus. C) Nuclear Nup62 integrity in N-SIM Super-resolution images was scored by blinded, unbiased observer. Scores are described in Supplemental Table 4. OptoTDP43+ cells received lower nuclear Nup62 integrity scores relative to control. D-E) Representative raw data from control (Cry-olig) and OptoTDP43 expressing cells shown in Fig 5D. F) Nup62 A.U.C. +Light. Cry2olig (blue bar) has an A.U.C. of ~0.5, while optoTDP43 (red bar) has a significantly lower A.U.C. of ~0.3 (p < 0.001, ***).

Corresponding images of nuclear Nup62 staining are shown above graph. F) Nuclear Nup62 fragmentation quantified according to intensity profile plots. Area under the curve (AUC) for Nup62 signal was averaged and expressed as a function of nuclear Nup62 circumference to account for variability in nuclear size. G) N-SIM Super-resolution images of Control (Cry2-oligo; top row) and OptoTDP43+ cells immunostained for Nup62 (green). Images revealed Nup62 sequestration into OptoTDP43 aggregates and this is highlighted by white box. Red signal depicts mCherry tag that is present on Cry2-Oligo and OptoTDP43 constructs. H) Representative image of FG nups being sequestered into optoTDP43 aggregates in Optofly model. FG nups, such as Nup62, were detected by MAb414 antibody in the ventral nerve cord of third instar larvae after 24h of blue-light stimulation. Arrows highlight optoTDP43 aggregates that co-stain for MAb414 while asterisks indicated optoTDP43 aggregates that are FG nup negative. In vitro sample size: n=7-10 cells/group. Statistical significance was determined by unpaired, twotailed t-test. * $p \leq 0.05$, *** $p \leq 0.001$ vs control. Scale bar: 2.5 μm (B), 10 μm (H)

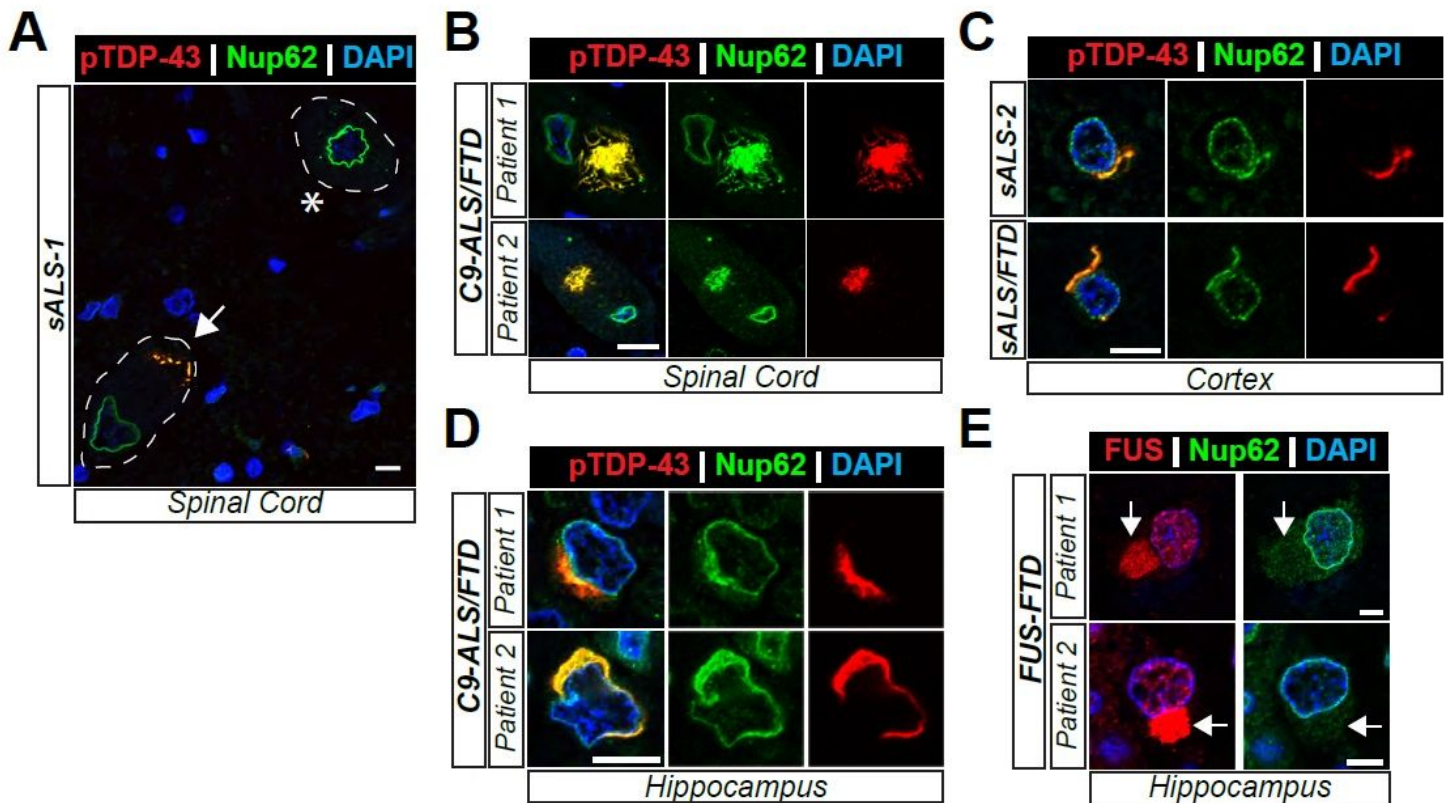


Figure 8

Nup62 colocalizes with pTDP-43 in C9-ALS/FTLD and sALS/FTLD Nup62 (green) and phosphoTDP-43 (red) immunoreactivity in postmortem tissue from various clinical diagnoses (noted above images and Supplemental Table 3). A-D) Intact nuclear Nup62 signal surrounds DAPI+ nuclei (asterisks) but becomes more diffuse in cells exhibiting cytoplasmic phosphoTDP-43 (arrowhead). Colocalization of Nup62 and phosphoTDP-43 accumulations were observed in the spinal cord (A & B), cortex (C), and hippocampus (D). Patient diagnostic classifications are described in Supplemental Table 3. E)

Cytoplasmic FUS accumulations (red, arrows) in the hippocampus from two FTLD patients do not show Nup62 localization. Scale bar: 10 μ m

Supplementary Files

This is a list of supplementary files associated with this preprint. Click to download.

- [ManuscriptSupTables.pdf](#)